ETH zürich

UQ STATE-DEPENDENT FRAMEWORK FOR SEISMIC FRAGILITY ASSESSMENT OF INDUSTRIAL COMPONENTS

C. Nardin, S. Marelli, O. S. Bursi, B. Sudret, M. Broccardo

CHAIR OF RISK, SAFETY AND UNCERTAINTY QUANTIFICATION
STEFANO-FRANSCINI-PLATZ 5
CH-8093 ZÜRICH

Risk, Safety & Uncertainty Quantification

Data Sheet

Journal:	-
Report Ref.:	RSUQ-2024-003A
Arxiv Ref.:	https://arxiv.org/abs/2405.04487 [stat.CO] [stat.AP]
DOI:	-
Date submitted:	May 7, 2024
Date accepted:	-

UQ state-dependent framework for seismic fragility assessment of industrial components

Chiara Nardin *[1], Stefano Marelli[2], Oreste S. Bursi[1], Bruno Sudret[2], and Marco Broccardo[1]

[1] *Department of Civil, Environmental and Mechanical Engineering, University of Trento, Italy*
[2] *Chair of Risk, Safety and Uncertainty Quantification, ETH Zürich, Switzerland*

May 7, 2024

Abstract

In this study, we propose a novel surrogate modelling approach to efficiently and accurately approximate the response of complex dynamical systems driven by time-varying Recently, there has been increased interest in assessing the seismic fragility of industrial plants and process equipment. This is reflected in the growing number of studies, community-funded research projects and experimental campaigns on the matter. Nonetheless, the complexity of the problem and its inherent modelling, coupled with a general scarcity of available data on process equipment, has limited the development of risk assessment methods. In fact, these limitations have led to the creation of simplified and quick-to-run models. In this context, we propose an innovative framework for developing state-dependent fragility functions. This new methodology combines limited data with the power of metamodelling and statistical techniques, namely polynomial chaos expansions (PCE) and bootstrapping. Therefore, we validated the framework on a simplified and inexpensive-to-run MDoF system endowed with Bouc-Wen hysteresis. Then, we tested it on a real nonstructural industrial process component. Specifically, we applied the state-dependent fragility framework to a critical vertical tank of a multicomponent full-scale 3D steel braced frame (BF). The seismic performance of the BF endowed with process components was captured by means of shake table campaign within the European SPIF project. Finally, we derived state-dependent fragility functions based on the combination of PCE and bootstrap at a greatly reduced computational cost.

*chiara.nardin@unitn.it

1 Introduction

1.1 Background and motivation

Assessing structural and non-structural component vulnerability to earthquakes is a key step in modern probabilistic seismic risk assessment Du et al. (2021). The PEER Performance-based earthquake engineering (PBEE) framework has gained significant momentum in this field, thanks to its inherently versatile formulation. Its strength lies in a simple yet effective implementation of the total probability theorem, which allows one to decouple and then combine the output of probabilistic seismic hazard analysis (PSHA) with fragility, damage, and loss analysis. To this end, the fragility analysis step offers the critical link between seismic hazard and structural modelling, since it estimates conditional probability of attaining or exceeding a specified damage state (DS), given an intensity measure (IM) of earthquake motion. Initially introduced for nuclear safety evaluation Richardson et al. (1980), fragility curves are nowadays widely used, ranging from assessment of collapse risk Eads et al. (2013) to loss estimation Rossi et al. (2020), from resilience quantification at individual scale Cimellaro et al. (2010) to community scale Burton et al. (2016), etc. In recent years, several novel methodological contributions to fragility analysis have been made. They include the development of multivariate fragility functions Du and Padgett (2020), the introduction of seismic fragility analysis based on a combination of real Gentile and Galasso (2020) and artificial ground motions and surrogate modelling Abbiati et al. (2021), and the consideration of both state Iervolino et al. (2015) and time-dependent fragility Di Maio et al. (2020), Ghosh and Padgett (2010). Nonetheless, the majority of the past research focus was committed to characterise the damage transition from a pristine state, i.e., no seismic damage, to a more severe damage state for structures subjected to a single ground motion Du and Padgett (2020), Gentile and Galasso (2020), Ghosh and Padgett (2010). Conversely, significantly less research has been devoted to state-dependent fragility modelling, which (i) can capture the damage accumulation due to sequential seismic events, and (ii) enables fragility estimations of structures with different initial damage states. To the best of our knowledge, only the first attempt has been made by Iervolino et al. (2015), Iervolino (2017), and Jia and Gardoni (2018). As a matter of fact, the compounding effect of damage accumulation and disruption caused by sequences of earthquakes (such as in Wenchuan (2008), Tohoku (2011) and central Italy (2016)), has highlighted the importance of accurately capturing the effect of irreversible damage accumulation for a reliable risk assessment. In this respect recent research, see, among others, Abdelnaby (2018) and Kassem et al. (2019), deeply investigated the effects of sequential seismic events and damage accumulation on the performance of RC frames, and computed the corresponding fragility curves. The results clearly demonstrated a substantial difference in seismic loss assessment. Similar conclusions are reached in Zhang et al. (2018) for fixed and base-isolated steel frame structures. In parallel, consistent procedures for selecting ground motions for event sequences have been the subject of thorough studies. Utilizing knowledge from prior work and literature, the authors in Zhang et al. (2018) provided recommendations for selecting record pairs

for sequential response history analysis and seismic performance assessment. In particular, the authors recommended the use of a seismic sequence (SS) of main-shock (MS) and after-shock (AS) record pairs, because they naturally capture and preserve within-sequence correlations. Besides, the use of SS-MS-AS record sets is preferred since databases with MS-AS records continue to expand and develop. However, to adequately populate the event sequences, ground motion models may serve the purpose. Advances in non-linear structural response simulations have yielded more accurate modelling of complex and multi-mode systems, allowing for gaining better insights into critical issues and performance behaviour of structures and installed non-structural components (NSCs). A more thorough discussion of these issues is reported in Quinci et al. (2023). Recently, significant efforts have been made to further investigate the coupling effects between the main structure and NSCs, both numerically Filiatrault et al. (2001) and De Biasio et al. (2015b), and experimentally Nardin et al. (2022), Mosqueda et al. (2009). An important milestone can be found in NIST GCR 17-917-44 (2017) that summarizes a year-long study, which collected and documented the body of available knowledge related to the seismic performance of NSCs for civil and industrial structures. Once again, since NSCs for industrial plants account for the majority of direct property losses due to earthquake damage Filiatrault et al. (2001), FEMA (2015), they were identified as a top priority in seismic risk assessment. However, to limit costly and disruptive non-structural damage is challenging, due to the need of predictive non-linear dynamic analysis for complex systems with strong coupling interactions with NSCs. They are mostly limited by available computational resources. In addition, the computation of fragility analysis requires a large number of non-linear time history analyses (NLTHA), limiting *de facto* the total number of possible simulations. This issue is central in simulation-based uncertainty quantification (UQ), which is tackled by replacing the computationally expensive NLTHA of FE models with an equivalent surrogate model, as in De Rocquigny et al. (2008), Sudret (2007), Sudret et al. (2017). In the context of fragility assessment, researchers have adopted different metamodelling techniques to offset the computational burden related to the large number of simulations needed. For example, the authors in Du et al. (2021) proposed a fragility modelling approach based on artificial neural networks for the initial and final damage classification. Moreover, Abbiati et al. (2021) adopted hierarchical Kriging to compute a multi-fidelity surrogate that fuses the predictions of multiple models for fragility assessment. Among the catalogue of families of surrogate models, polynomial chaos expansions (PCE) Blatman and Sudret (2008), Bayesian networks Lu and Zhang (2021), support vector machines Hurtado (2007), and artificial neural networks Roy and Chakraborty (2023) have arguably become the most popular in civil engineering, since they provide more than just an approximation to the underlying computational model. In particular, they additionally yield analytical estimates of the response moments of the model, sensitivity indices or confidence levels for their own predictions. For example, Zhu et al. (2023) estimated the full conditional probability distribution of EDP conditioned on IMs by means of stochastic PCE. An in-depth literature review of the current state-of-the-art in surrogate modelling for reliability assessment is presented in Teixeira et al. (2021) and Moustapha et al. (2022). Undoubtedly, one of the most significant benefits of surrogate models is their

computational efficiency after training, allowing for millions of model evaluations per second, even on common end-user hardware. This enables the estimation of empirical fragility functions, as addressed in the literature by the global earthquake model (GEM) Rossetto et al. (2015) and Ioannou et al. (2012).

1.2 Scope and core contribution

On these premises, this paper presents a novel UQ-based framework for efficiently deriving state-dependent fragility curves of industrial system components. This approach blends data from a reduced number of complex and expensive sequential NLTHAs with cutting-edge metamodelling techniques. In detail, the paper is organised as follows. In Section 2, we present the heuristics and the novel framework for state-dependent fragility assessment. In Section 3, we validate the methodology on an inexpensive-to-evaluate benchmark case study. Specifically, state-dependent fragility functions derived from brute-force Monte Carlo Simulation (MCS) are compared with surrogate-based MCS. In Section 4, we applied the framework to a real industrial case study. Precisely, the case study deals with a critical non-structural component (NSC) installed on the steel braced frame (BF) substructure, i.e. a vertical tank, as part of the project SPIF (Nardin et al. (2022)). Finally, we provide in Section 5 a summary of the main findings as well as future development perspectives.

2 A state-dependent fragility analysis framework

Limited by the availability of time and information, risk-informed assessments are commonly carried out on the basis of simplified and quick-to-evaluate models. However, as highlighted in the recent NIST GCR 17-917-44 (2017) report devoted to industrial facilities, these proven strategies lead to neither economically viable nor rational designs. On these premises, this Section presents the heuristic of a novel framework for system vulnerability assessment. Specifically, based on a combination of experimental data and surrogate models, the proposed methodology enables the computation of state-dependent fragility curves that consider several aspects of the problem.

State-dependent fragility curves are defined as a class of fragility curves conditioned not only by a measure of seismic intensity **IM** (which in generalised form is a vector), but also by the initial state of (discrete) damage $\mathrm{DS_i}$ of the structure (see, Iervolino et al. (2015)). Hence, state-dependent fragilities enable the assessment of the vulnerability of a system that has already experienced damage, as defined by the generalised equation:

$$\mathbb{P}\Big[\mathrm{DS_j}|\mathrm{DS_i},\, \boldsymbol{IM}=\boldsymbol{im}\Big] = \mathbb{P}\Big[\mathrm{DS}\geq \mathrm{DS_j}|\mathrm{DS_i},\, \boldsymbol{IM}=\boldsymbol{im}\Big] - \mathbb{P}\Big[\mathrm{DS}\geq \mathrm{DS_{j+1}}|\mathrm{DS_i},\, \boldsymbol{IM}=\boldsymbol{im}\Big], \tag{1}$$

for $j > i$, and i indices ranging among the identified and most severe damage limit states. Figure 1(a) shows the generalised transition probability state matrix for a system with three

possible levels of damage, i.e., DS_0 to DS_2. Each row of the matrix represents the initial damage state or level; whilst each column indicates the final damage state. Each bin represents the transition probability between the initial (row) and final (column) state, including the permanence within the same level. The lower triangular part of the matrix represents the recovery processes of the investigated system, which, for brevity, we do not consider in this paper. Moreover, the ultimate damage limit state DS_2 is considered an absorption state, i.e., a condition that, cannot be exited or recovered once reached. A typical example would be the collapse of the structural system. Similarly, Figure 1(b) shows the Markovian diagram underlying the transition state matrix, e.g., the allowable jumps between the three-level damage states.

Transition to damage state DS_i

Initial damage state Ds_i	$\mathbf{DS_0}$	$\mathbf{DS_1}$	$\mathbf{DS_2}$
$\mathbf{DS_0}$	$1 - \mathbb{P}_{01} - \mathbb{P}_{02}$	$\mathbb{P}[DS \geq DS_1 \mid DS_0, IM] - \mathbb{P}[DS \geq DS_2 \mid DS_0, IM]$	$\mathbb{P}[DS \geq DS_2 \mid DS_0, IM]$
$\mathbf{DS_1}$	✕	$1 - \mathbb{P}_{12}$	$\mathbb{P}[DS \geq DS_2 \mid DS_1, IM]$
$\mathbf{DS_2}$	✕	✕	1

(a)

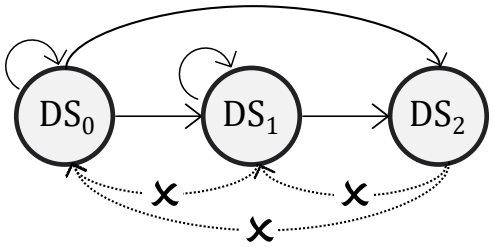

(b)

Figure 1: Transition state (a) matrix and (b) diagram, respectively.

State-dependent fragility analysis requires a vast number of NLTHAs because each position of the transition matrix needs to be sufficiently populated. As a consequence, time histories of multiple seismic events, e.g., seismic sequences, are cast and applied as input for the NLTHAs. This enables us to cover each transition state and different damage initial configurations effectively. Then, the structural and non-structural system performances are clustered according to the damage reference metric. Hence, either empirical or parametric fragility functions are derived, conditioned on the initial damage state condition and the **IM** of the seismic input. Figure 2 describes the fundamental steps of the workflow, i.e., from the FE and seismic input models definition (steps $\mathcal{A} - \mathcal{B}$) to the complete NLTHAs and fragility computations (step $\mathcal{C}$). However, when considering realistic computational models, the significant computing demands of an extensive set of sequential NLTHAs generally hinder this direct derivation of state-dependent

fragilities, as in step $\mathcal{C}$ upper-right corner of Figure 2. To tackle this limit, the global UQ framework developed in Sudret (2007) and Sudret (2008) is adapted in the proposed methodology. The following three steps are used to define the UQ problem: (i) step $\mathcal{A}$, i.e., the definition of the computational model $\mathcal{M}(\cdot)$; (ii) step $\mathcal{B}$, description of the input parameters; (iii) step $\mathcal{C}$, propagation of the uncertainties and processing of the quantities of interests (QoIs). Specifically, in the proposed framework, for the steps $\mathcal{A}-\mathcal{B}$, we first perform a given number of sequential NLTHAs:

$$\mathcal{Y} = \mathcal{M}(\mathcal{X}) = \mathcal{M}_{FE} \circ A(t, \mathcal{X}) = \mathcal{M}_{FE}\left(A(t, \mathcal{X})\right), \tag{2}$$

where $A(t, \mathcal{X})$ is a given seismic sequence generated by a stochastic site-based ground motion model (GMM), and $\circ$ represents the function composition. $\mathcal{X}$ is a high-dimension random vector which represents both the epistemic (i.e., the stochastic nature of the model parameters), and the aleatory uncertainties (i.e., the Gaussian random variables representing the Gaussian noise). Specifically, $\mathcal{X} = [\mathcal{X}_1, \ldots, \mathcal{X}_j, \ldots \mathcal{X}_M]^T$, where $\mathcal{X}_j$ is a random vector which represents the stochastic nature of a given ground motions (gms) and M the total number of seismic events that constitute the seismic sequence. Moreover, $\mathcal{M}_{FE}(\cdot)$ represents the expensive-to-run FE model; $\mathcal{Y}$ a random vector that collects the QoIs of the case study. In particular, $\mathcal{Y} = [\mathcal{Y}_1, \ldots, \mathcal{Y}_j, \ldots \mathcal{Y}_M]^T$, where $\mathcal{Y}_j$ is the time series response of the associated $\mathcal{X}_j$ random seismic event.

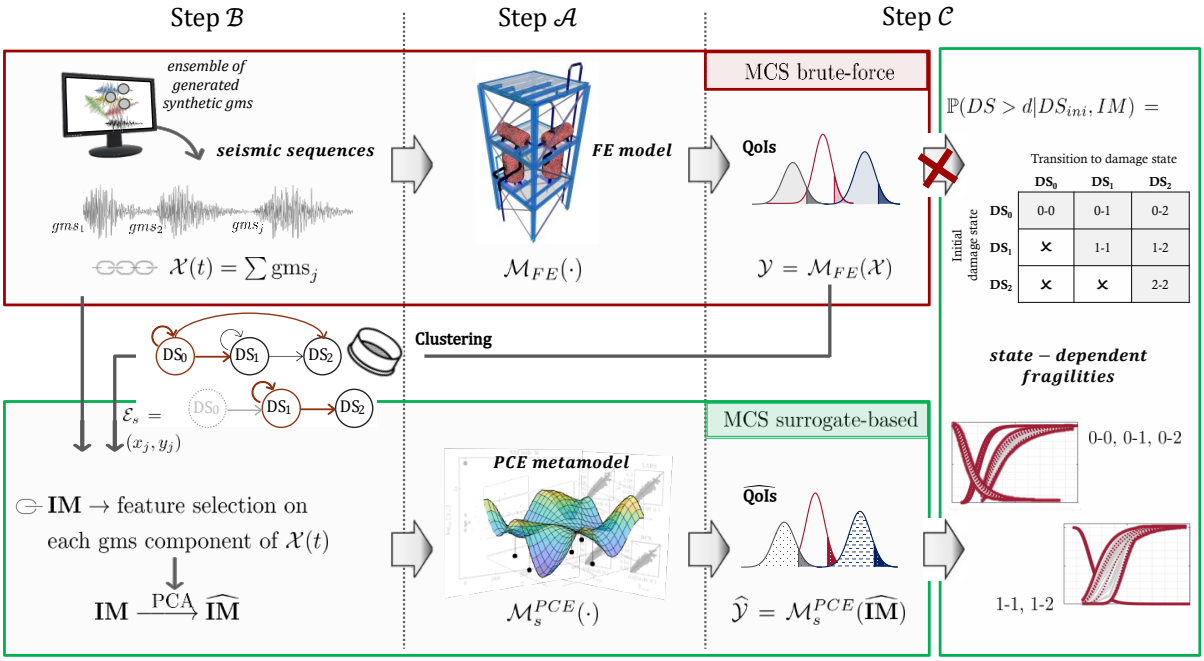

Figure 2: UQ-based framework and key steps for performing state-dependent fragility analysis. The top red-contoured row displays the brute-force MCS path on expensive-to-run NLTHAs (step $\mathcal{A}$ to $\mathcal{C}$), while the green one embeds the surrogate-based MCS method. Specifically, for the top row, complex and computationally demanding FE models are developed in step $\mathcal{A}$; whilst, in step $\mathcal{B}$, a GMM is deployed to compose stochastic seismic sequences to assign as input. However, the computational burden hinders the allowable number of MCS. This results in a constraint to the derivation of state-dependent fragility functions, as highlighted by the interrupted red-crossed arrow. Nevertheless, the obtained limited NLTHAs QoIs are clustered according to the damage initial state metric $\text{DS}_{0,1,2}$. Those clustered data, coupled with the corresponding seismic event of the sequence, constitute the DoE $\mathcal{D}_s$ for the surrogate models (step $\mathcal{A}-\mathcal{B}$). First, a comprehensive vector of $\boldsymbol{IM}$s is extracted. Then, PCA is applied to limit the dimensionality of the input. This allows us to set PCE metamodels for each $\mathcal{D}_s$, $s \in [\text{DS}_0, \text{DS}_1]$. Finally, a vast number of surrogate-based MCS enables the derivation of state-dependent fragilities, (step $\mathcal{C}$).

Next, instead of expensive-to-run FE models, cost-effective metamodels for each initial damage level—i.e., rows of the transition matrix of Figure 1(a)—are tailored on the physics-informed problem and trained on a much smaller dataset. In particular, the QoIs resulting from the NLTHAs are clustered according to the predefined damage initial states, i.e., the number of rows of the transition state matrix of Figure 1(a). For clarity, only the allowable transition state jumps are sketched. The clustering determines the pairs of $(\mathbf{x}_j, y_j)$, where j identifies each gm of the seismic sequences. This step serves to define different designs of experiment (DoE) depending on the initial state of the structure. Specifically, we identify the different DoEs with $\mathcal{D}_s$, where s identifies the initial state of the structure, i.e., $s \in \{\text{DS}_0, \text{DS}_1\}$. In the following step, a low-dimensional input representation is used instead of the time series sequences to build a time-invariant surrogate model. Specifically, we used a vector of $\mathbf{IM}_j$,

following the classical approach of vector-PSHA analysis. Besides the most popular IMs such as PGA and PGV, novel and less widespread IMs have also been introduced. Among them: the $I_{RG,a}$ Riddell–Garcia Intensity acceleration and velocity measures, which minimise dispersion of hysteretic energy-dissipation spectra of inelastic systems; the I_F Fajfar Intensity, a compound IM that takes into account the damage capacity of medium-period structures; and the E-$ASA_{R,x}$ equipment relative average spectral acceleration, introduced in De Biasio et al. (2015b). The last one is of particular interest since it allows us to consider shifts in the frequency range of the structure due to damage experienced by the installed equipment. The Table 1 enlists the considered 41 IMs. Since among the list of IM several of them are strongly correlated, we seek specific patterns that allow dimensionality reduction. Therefore, we perform principal component analysis (PCA), to obtain a low dimension vector $\widehat{\mathbf{IM}}_j$, which can be interpreted as a vector of uncorrelated pseudo-IMs.

Particularly, PCA was used to select the least number of principal components (PCs) to satisfactorily characterise $\widehat{\mathbf{IM}}$. Finally, we build PCE surrogate models based on the pairs $(\widehat{\boldsymbol{im}}_j; y_j)$:

$$\widehat{\mathcal{Y}} = \mathcal{M}_s^{PCE}\left(\widehat{\boldsymbol{IM}}\right), \tag{3}$$

where $\mathcal{M}_s^{PCE}(\cdot)$ is the PCE surrogate model; $\widehat{\mathcal{Y}}$ is the vector collecting the surrogated QoIs; $s \in [\mathrm{DS}_0; \mathrm{DS}_1]$ identifies the initial state of the structure. The vast number of MCS surrogate-based analyses enables us to derive non-parametric state-dependent fragilities functions, as defined in Eq. 1. Moreover, notice that the framework is not intrusive, meaning that the complex FE model is completely decoupled from the UQ analysis. This allows FE experts to work independently from UQ experts. In the following Sections, the proposed UQ-based framework is applied twice. Specifically, in Section 3 on an inexpensive-to-run benchmark case study, to validate the methodology and to illustrate its key steps and tools. Then, in Section 4, we derive state-dependent fragility functions for a vertical tank installed on the industrial mock-up of the SPIF project.

3 Benchmark case: Hysteretic MDoF system

To test the validity of the proposed framework, we examine the case of an equivalent mechanical cheap-to-evaluate multiple-degree-of-freedom (MDoF) shear-type system with Bouc-Wen hysteresis. This allows us: (i) to perform a vast number of sequential NLTHAs, and (ii) to evaluate state-dependent fragilities in terms of the inter-storey drift ratio (ID-ratio). Then, the MCS brute-force fragilities are quantitatively and qualitatively compared with the surrogate-based MCS fragilities, derived by applying the UQ-based framework of Section 2.

3.1 Step $\mathcal{A}$ - Computational model description

According to the scheme depicted in Figure 2, the MDoF system belongs to step $\mathcal{A}$ of the framework, i.e., the definition of the numerical model. The benchmark case study is a 2D

Table 1: A comprehensive list of ground motion IM parameters De Biasio et al. (2015b) - Hariri-Ardebili and Saouma (2016).

No.	Description of IM	Symbol	Units	Mathematical model
1	Peak ground acceleration	PGA	[m/s^2]	$\max(\lvert\ddot{u}(t)\rvert)$
2	Peak ground velocity	PGV	[m/s]	$\max(\lvert\dot{u}(t)\rvert)$
3	Peak ground displacement	PGD	[m]	$\max(\lvert u(t)\rvert)$
4,..,8	Spectral displacement	Sd	[m]	$S_d(T_x)$
9,..,13	Spectral velocity	Sv	[m/s]	$S_v(T_x)$
14,..,18	Spectral acceleration	Sa	[m/s^2]	$S_a(T_x)$
	* *where* $T^* \in [0.50; 0.35; 0.25; 0.15; 0.10]$			
19	Arias intesity	I_A	[m/s]	$\pi/2g \cdot \int_0^{t_f} a^2(t)\mathrm{d}T$
20	Total cumulative energy	E_{cum}	[m^2/s^3]	$\int \ddot{u}^2(t)\mathrm{d}t$
21	Riddell–Garcia Intensity Acceleration	$I_{RG,a}$	[m/s$^{5/3}$]	$(PGA)^{+1} \cdot (T_d)^{+1/3}$
22	Riddell–Garcia Intensity Velocity	$I_{RG,v}$	[m$^{2/3}$/s$^{1/3}$]	$(PGV)^{+2/3} \cdot (T_d)^{+1/3}$
23	Significant time duration	T_d	[s]	$t_{95} - t_{05}$
24	Root mean square of acceleration	RMS($\ddot{u}\,(t)$)	[m/s^2]	$\sqrt{(\frac{1}{N}\sum_{n=1}^{N}\lvert x_N^2\rvert)}$
25	Characteristic intensity	IC	[m$^{3/2}$/s$^{3/2}$]	$\mathrm{RMS}(\ddot{u}(t))^{1.5} \cdot T_d^{0.5}$
26	Cumulative absolute velocity	CAV	[m/s]	$\int_0^{t_f} \lvert a(t)\rvert \mathrm{d}T$
27	Cosenza–Manfredi Intensity	I_{CM}	[–	$2g/\pi \cdot (PGA)^{-1}(PGV)^{-1}(AI)^{+1}$
28	Average spectral acceleration	ASA_{40}	[m/s]	$2.5/f_1 \int_{0.6 \cdot f_1}^{f_1} S_a(f,\varepsilon)\mathrm{d}f$
29	Acceleration spectral intensity	ASI	[m/s^2]	$\int_{0.1}^{0.5} S_a(T,\varepsilon)\mathrm{d}T$
30	Effective peak acceleration	EPA	[m/s^2]	$1/2.5 \int_{0.1}^{2.5} S_a(T,\varepsilon)\mathrm{d}T$
31	Velocity to acceleration ratio	$I_{v/a}$	[s]	PGV/PGA
32	Fajfar Intensity	I_F	[m/s$^{3/4}$]	$(PGV)^{+1} \cdot (T_d)^{+1/4}$
33	Mean frequency	F_m	[1/s]	$\sum_i U_i^2(f_i)/\sum_i U_i^2$
34	Rate of change mean frequency	$\dot{F}_m$	[–]	$\mathrm{d}F_m(T)/\mathrm{d}t$
35	Fourier amplitude spectrum area	FAS_{area}	[m/s^2]	$\frac{1}{4df} \int_{f_1-2df}^{f_1+2df} U(f)\mathrm{d}f$
36,..,41	Equipment relative average spectral acceleration	E-$ASA_{R_xx}^{**}$	[m/s^2]	$\frac{1}{f_1 \cdot (X_f - 1)} \cdot \int_{f_1}^{X_f \cdot f_1} S_a(f,\varepsilon)\mathrm{d}f$
	** *R indicates the chosen percentage of drop of the fundamental frequency* ($X_f = 1 - (R/100)$)*;*			
	$R \in [40; 67; 80; 100; 150; 200]$			

condensation of the complex 3D industrial frame, namely SPIF #2 system. Conversely, the full 3D system is studied in Section 4.1. The SPIF #2 project focused on investigating the seismic

behaviour of a prototype multi-storey BF structure equipped with complex secondary industrial components by means of shaking table tests. More details on the project can be found in Quinci et al. (2023), whilst the shake table test campaign and system performance are described in Nardin et al. (2022). The primary objective of the MDoF model is to efficiently capture the displacement and shear response time histories at each floor level of the complex BF system. To allow the execution of a significant number of NLTHAs, a strong emphasis on minimizing the computational resources and time is devoted. In this context, the engineering demand parameter (EDP) is represented by the maximum ID-ratio. Thus, according to Table C1-3 *Structural Performance Levels and Damage* of FEMA 356 Agency (2000), the identified damage metrics DS_i are 0.5% and 2.0% of the ID-ratio, for Immediate Occupancy (IO) and Collapse Prevention (CP) limit states, respectively. The numerical model implemented in-house with MATLAB© is defined by the semi-discretised system of equations of motion,

$$\mathbf{M}\,\ddot{u} + \mathbf{C}\,\dot{u} + \mathbf{K}\,[\alpha u + (1-\alpha)\,z] = -\mathbf{M}\,\ddot{u}_g, \tag{4}$$

where the stochastic base input $\ddot{u}_g$ is a realization of the process $A\,(t, \mathcal{X})$, later on presented in Eq. 6 of Section 3.2. Both the mass $\mathbf{M}$ and the stiffness $\mathbf{K}$ matrices are calculated from the experimental data collected during the SPIF #2 test campaign Nardin et al. (2022); while, the damping $\mathbf{C}$ is set to match a viscous damping ratio of 4.5%, as detailed in Quinci et al. (2023). The $\{\alpha, \beta_N, \gamma_N, \delta D, \delta\nu, \delta\eta, z\}$ terms related to the Bouc-Wen hysteresis follow the formulation presented in Haukaas and Der Kiureghian (2003), summarized as:

$$\dot{z} = \frac{\mathbf{D}\,\dot{u} - \{\beta|\dot{u}|z|z|^{n-1} + \gamma|z|^n\dot{u}\}\cdot\nu}{\eta}. \tag{5}$$

All system parameters are reported in Table 2, whilst Figure 3 depicts the comparison of the hysteresis at the top level for the reduced MDoF Bouc-Wen-based model versus the full FE BF model under seismic excitation.

Table 2: Bouc-Wen parameters for the MDoF system.

Parameter		**Value**
α, n, β_N,γ_N	[-]	[0.01; 1.5;0.167; 0.50]
δD,$\delta\nu$,$\delta\eta$	[-]	[0.002; 1.00; 1.00]E-08
K_0	[N/m]	[1.72;1.77;0.96]E+07
M	[kg]	[9.5;14.5;12.4]E+03

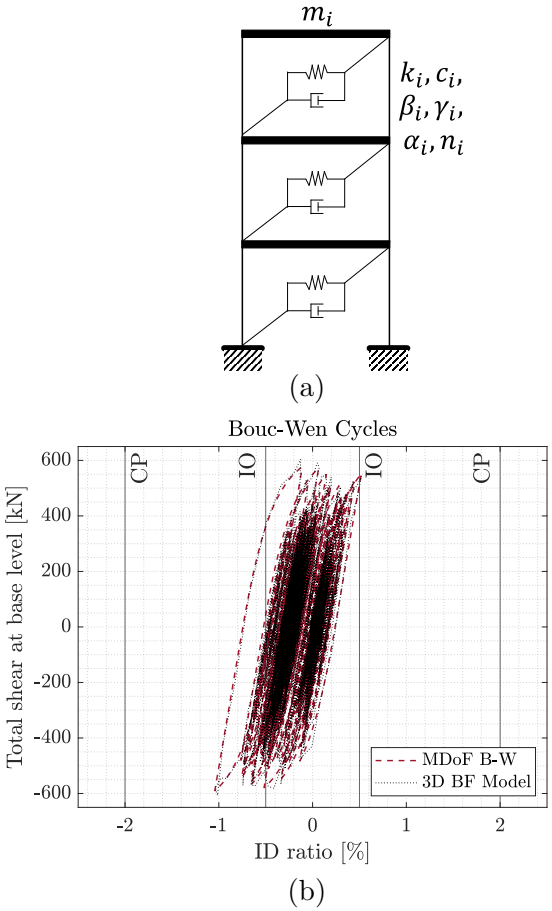

Figure 3: (a) Schematics of the 2D MDoF system; (b) comparison of the hysteretic cycles at the top level of the 2D MDoF and the 3D BF model.

3.2 Step $\mathcal{B}$ - Input definition

Sequential chains of seismic events derived from the site-based GMM of Rezaeian and Der Kiureghian (2010) are used as the excitation. We consider the far-field GMM scenario described in Nardin et al. (2022) for the experimental test campaign of SPIF #2. Briefly, the GMM is based on a modulated and filtered discretized white-noise process described by the following equation:

$$A\left(t,\mathcal{X}\right) \;=\; q\left(t,\boldsymbol{\Theta}_q\right)\left[\frac{\sqrt{2\pi S\Delta t}}{\sigma_h(t)}\sum_{l=1}^{k} h\left[t-t_l,\boldsymbol{\Theta}_h(t_l)\right]\cdot Z_l\right] \;\text{ with }\; t_k \le t < t_{k+1}, \tag{6}$$

where $q(t,\boldsymbol{\Theta}_q)$ is the modulating function, Z_l denote the standard normal Gaussian Random Variables, and $\sigma_h^2 = 2\pi S\Delta t\sum_{l=1}^{k} h^2[t-t_l,\theta(t_l)]$ the standard deviation of the discrete filtered white-noise process. Moreover, t_l is a set of equally spaced time points (with $l = 0, 1, ..., L$, $t_0 = 0$, and t_L representing the total duration of the motion) and $k = \text{int}(t_L/\Delta t) = 0, 1, \ldots, L$. As shown in Rezaeian and Der Kiureghian (2010), $\boldsymbol{\Theta}_q = [I_a, t_{mid}, D_{5-95}]$ are the parameters of the modulating function, while $\boldsymbol{\Theta}_h = [\omega_{mid}, \dot{\omega}, \zeta]$ are the filter parameters. Provided with this representation, $\boldsymbol{\mathcal{X}}$ (in Eq. (2)) is written as follows $\boldsymbol{\mathcal{X}} = [I_a,\, D_{5-95},\, t_{mid},\, \omega_{mid},\, \dot{\omega}_{mid},\, \zeta_f, Z_1, \ldots, Z_L]$. Observe that $\boldsymbol{\mathcal{X}}$ includes both an aleatory component represented by the Gaussian random variables

and an epistemic component represented by the randomized GMM parameters. The marginal distributions of the GMM parameters are summarized in Table 3. In Nardin et al. (2022), these distributions were inferred from selected INGV and ITACA datasets based on the following assumptions: (i) distance fault-site $R > 10$[km]; (ii) moment magnitude $M_w > 5.5$; (iii) main shock seismic events only; (iv) strong motion intensities expressed in terms of $PGA > 0.075$[g]. The complete list of the selected natural records and their characteristics is provided in Nardin et al. (2022). Then, the calibrated GMM is used to generate an ensemble of 10^4 simulated ground motions (gms). Based on the following assumptions: (i) mainshock events characterized by long return periods, (ii) no recovery/restoring processes, and (iii) negligible degradation effects with respect to seismic damage, gms are randomly extracted from the generated synthetic gms ensemble to compose sequences of seismic time histories, as sketched in Figure 2-Step $\mathcal{B}$. Observe that we do not consider after-shock sequences, but only sequences of main shock events. Next, we construct the dataset in the following way. We simulate 10^4 gms and then we randomly generate a sequence of 10 seismic events by randomly permuting the 10^4 gms. Thus, the resulting artificial dataset comprises 10^3 sequences of 10 gms. Finally, we reproduce 100 of such datasets. In particular, the generation of the GMM parameters is sampled using the 100 predefined seeds (for reproducibility). Notice that the white noise is not reproducible. The adoption of earthquake sequences allows for considering seismic damage accumulation through time, thus mimicking the effect of non-pristine initial conditions on the structure.

Table 3: Probabilities density distributions of the parameters of the site-based GMM.

Model Parameters		**Units**	**Distribution**	$\boldsymbol{\mu}$	$\boldsymbol{\sigma}$	**Distribution Bounds**
I_a	Arias Intensity	[m/s]	Log-normal	-0.46	0.51	$(0; +\infty)$
D_{5-95}	Time interval of 95% of the I_a	[s]	Log-normal	2.21	0.23	$(0; +\infty)$
t_{mid}	Time interval of 45% of the I_a	[s]	Log-normal	1.698	0.21	$(0; +\infty)$
$\omega_{mid}/2\pi$	Filter frequency at t_{mid}	[Hz]	Uniform	4.8	1	$[3.8; 5.8]$
ζ_f	Filter damping ratio	[-]	Uniform	0.35	0.1	$[0.25; 0.45]$

*$\dot{\omega}_{mid}$, *rate of change of frequency with t, is assumed constant and equal to -0.5*

3.3 Step $\mathcal{C}$ - QoI response

3.3.1 Brute-force MCS for state-dependent fragility functions

A total amount of 10^6 sequential NLTHAs were performed, thanks to the minimal computational effort required by a single sequential NLTHA[1]. For each simulation, the initial and final damage configurations were identified based on the EDP. Next, simulations were clustered according to the initial and the final damage state level associated with each ground motion of the seismic

[1] ≈3s on an Intel(R) Core(TM) i9-10900K CPU @3.70GHz, 10 Core(s) - 128 GB RAM

sequence, as in Figure 4. Thus, six combinations among initial-final damage configurations are possible: '0-0' , '0-1' , '0-2' , '1-1' , '1-2' , '2-2'. Those represent the transition states of the system, as sketched in Figure 1(a). Specifically, the '0-0' , '0-1' , '0-2' identify, given a pristine DS_0 initial state condition, the permanence in the DS_0 and transition to damage state level DS_1 and DS_2, respectively. Similarly, '1-1' ,'1-2' identify the permanence in DS_1 and transition to damage state level DS_2, given an initial damage state level DS_1. Finally, the '2-2' refers to the absorption state of collapse.

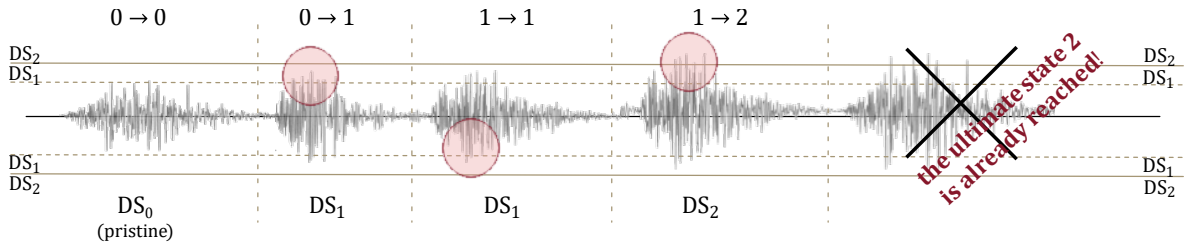

Figure 4: Example of seismic sequence time history response clustered according to the initial and final damage state level, e.g., ranging from DS_0 (pristine) to DS_2 (collapse).

Table 5(a) collects the numbers of clustered results of the MCS, while Table 5(b) the percentages. Nearly 74% of the total simulations exhibited an initial damage level of DS_1, with approximately 70% concentrated within the '1-2' cluster. Conversely, around 20% of simulations were performed with no initial damage, e.g., DS_0. The remaining 6% of simulations resulted in an absorption collapse state. According to Eq. 1, to evaluate state-dependent fragilities, an optimal IM, or a

Transition to damage state

Initial damage state	DS_0	DS_1	DS_2
DS_0	100162	84335	11359
DS_1	×	40349	705980
DS_2	×	×	57815

#no. of sim. for each initial − final damage state level cluster

(a)

Transition to damage state

Initial damage state	DS_0	DS_1	DS_2
DS_0	10%	8.4%	1.1%
DS_1	×	4.0%	70.6%
DS_2	×	×	5.8%

% of sims. for each initial − final damage state level cluster

(b)

Figure 5: Transition state matrices: (a) counters and (b) percentages of simulation for each initial-final damage state level cluster, respectively.

vector of optimal IMs, needs to be defined. To do so, we implemented an efficiency criterion β_{eff} based on Hariri-Ardebili and Saouma (2016) and Zentner et al. (2017). Based on Figure 6, first, we determine the $x_q = 25^{th} - 50^{th} - 75^{th}$ quantiles of each marginal IM distribution of Table 1. Second, we evaluate the 90^{th} inter-quantile range IQR in correspondence with the previous quantiles of the marginal IM distributions. Third, we sum these 90^{th} IQR ranges. Finally, the

optimal β_{eff} is the minimum among the IM_i. Eq. 7 describes the criterion:

$$\beta_{\text{eff}}(IM_i) = \min\left(\sum_{x_q} \text{IQR}_{x_q}(IM_i)|_{0.10}^{0.90}\right), \tag{7}$$

with IM_i ranging across the 41 elements of the vector $\boldsymbol{IM}$ defined in Table 1. Next the optimal IM is selected as follow $IM^* = \text{argmin}_{IM_i}\ \beta_{\text{eff}}(IM_i)$. This procedure is applied for each transition state. It follows that transitions can have different optimal IM^*s. The collection of the optimal transition IM^*s defines the optimal vector $\boldsymbol{IM}^*$, which is used to construct state-dependent fragility functions. At this stage, brute-force MCS on cheap-to-evaluate systems allows us to reach a full probabilistic description of fragilities. Given the vast number of simulations, empirical fragilities were evaluated for each transition state. Specifically, non-parametric curve-fitting on the cumulative distributions of data against the optimal IM was implemented, as in Rossetto et al. (2015).

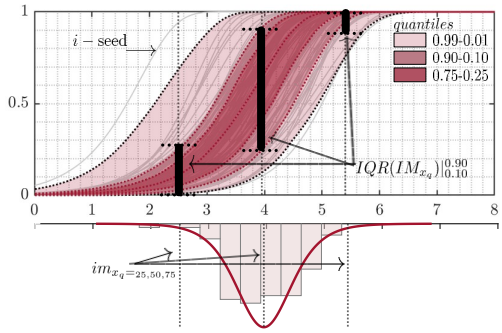

Figure 6: β_{eff} criterion explained: step (i), determine the $x_q = 25^{th} - 50^{th} - 75^{th}$ quantiles on the marginal IM; step (ii), evaluate the $\text{IQR}|_{0.10}^{0.90}$ on x_q; step (iii), repeat $\forall IM_i$ and find the minimum.

Figure 7 represents the collection of state-dependent fragility functions based on IM^*. Notice that this Figure does not represent the transition matrix defined in Eq. 1. In fact, this is used to highlight the components of $\boldsymbol{IM}^* = [PGA,\ I_{RG,a},\ ASI,\ E-ASA_{R80}]$. Each one of the 100 MCS seeds is associated with a grey line. The curves representing the 90% confidence bounds are displayed in a dashed-dotted dark red style, while those for the 50% confidence bounds are represented with dashed lines. The first row, corresponding to a pristine initial damage state condition, is characterized mainly by PGA-derived IMs, while the second row is characterized by S_a-related features. Furthermore, it becomes evident that the optimal IM changes as moving toward more severe damage states or starting from a non-pristine initial condition. Particularly, the evolving IM is characterized by features capable of capturing reductions in stiffness due to the accumulation of damage, and shifts in the frequency range of the structure, such as E-ASA_{R^*}. The β_{eff} values are collected in Table 4. A limitation of this approach is that one needs to develop a fragility model based on $\boldsymbol{IM}^*$, which can become computationally demanding (in terms of memory allocation). In this specific example, the state-dependent fragility models,

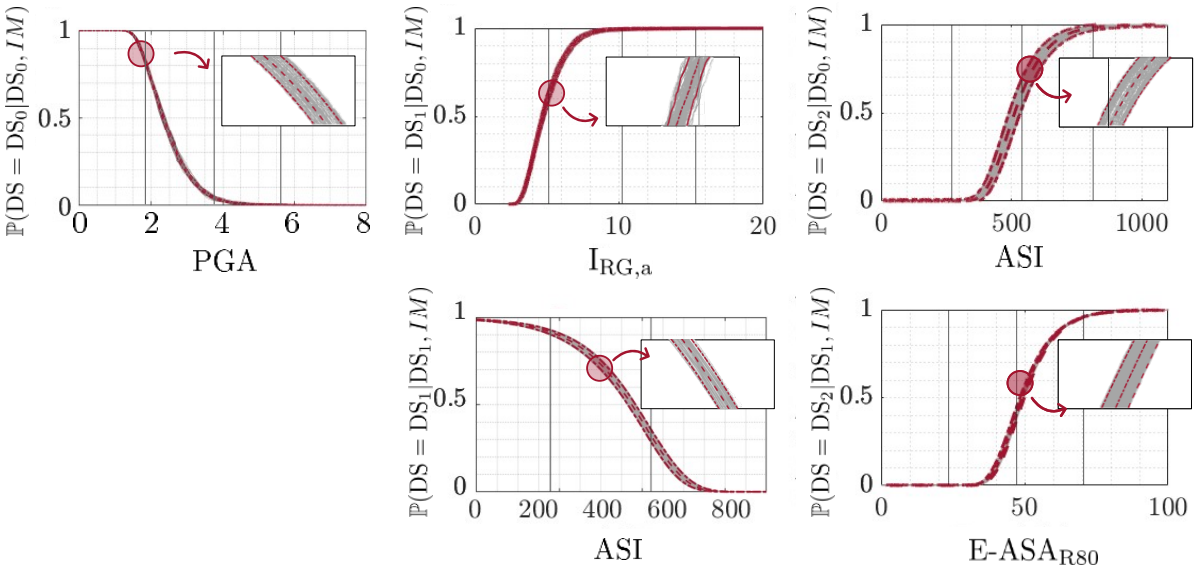

Figure 7: Brute-force MCS state-dependent fragility functions: grey lines represent single seed simulations; dashed-dot dark-red lines depict the 90% confidence bounds, whilst dashed-dark red ones the 50%. Different IMs are adopted in x-axes, according to the optimal β_{eff} for each transition state.

Table 4: Brute-force MCS state-dependent fragility functions: top five β_{eff} efficiency indices for each transition state.

Frag. '0-0' Optimal IM	β_{eff} **index**	**Frag. '0-1' Optimal IM**	β_{eff} **index**	**Frag. '0-2' Optimal IM**	β_{eff} **index**	**Frag. '1-1' Optimal IM**	β_{eff} **index**	**Frag. '1-2' Optimal IM**	β_{eff} **index**
PGA	9.60E-02	$I_{RG,a}$	1.83E-02	ASI	8.59E-02	ASI	7.00E-03	E-ASA$_{R80}$	1.96E-02
IC	1.01E-01	PGA	2.10E-02	EPA	9.55E-02	EPA	7.70E-03	E-ASA$_{R200}$	2.24E-02
$I_{RG,a}$	1.03E-01	$I_{RG,v}$	2.50E-02	RMS(ü)	9.82E-02	PGA	7.70E-03	E − ASA$_{R100}$	2.31E-02
E-ASA$_{R80}$	1.07E-01	E-ASA$_{R80}$	2.62E-02	PGA	9.83E-02	$I_{RG,v}$	7.90E-03	E-ASA$_{R150}$	2.63E-02
RMS(ü)	1.10E-01	PGD	2.63E-02	E-ASA$_{R80}$	1.17E-01	$I_{RG,a}$	8.10E-03	$I_{RG,a}$	4.10E-02

$\mathbb{P}(\text{DS}_j|\text{DS}_i, \boldsymbol{IM}^*)$ are four-dimensional functions. Moreover, a vector-based seismic risk analysis needs to be developed to use this model directly. While this is not a limit in a Monte-Carlo-based seismic risk analysis, it becomes prohibitive for direct integration. A more straightforward approach is to use state-dependent fragilities as functions of one optimal IM for the entire transition states. This is especially convenient when performing risk assessment since it allows the use of directly available GMPEs. Therefore, we proposed a global efficiency metric defined as

$$\beta_{\text{eff,glob}}(IM_i) = \min\left(\sum_{s=0}^{S} \frac{\beta_{\text{eff}}(IM_i)|_s}{\left(\sum_j^{41} \beta_{\text{eff}}(IM_j)\right)|_s}\right), \quad \forall IM_i \in \mathbf{IM} \,\text{and}\, s = \{0, \ldots, S\} \tag{8}$$

where s represents the allowable transition states, e.g., '0-0','0-1','0-2','1-1','1-2'. Specifically, we first normalize the β_{eff} index for each transition state over the i to 41 IMs. Then, we sum the same IM_i across the transition states, and, finally, we select the minimum. Table 5 gathers the global ranking for optimal IMs.

	Global Optimal IM	$\beta_{\text{eff,glob}}$ index[%]
1.	PGA	9.12
2.	PGD	9.20
3.	E-ASA$_{\text{R800}}$	9.21
4.	I$_{\text{RG,a}}$	9.39
5.	Sa(T$_1$)	9.49

Table 5: Ranking of the optimal IMs according to the global $\beta_{\text{eff,glob}}$, defined in Eqn. 8.

Figure 8 shows the probabilistic description of state-dependent fragilities as functions of the global optimal IM, i.e., the PGA. According to the definition of Eq. 1, Figure 8 reproduces the transition matrix of Figure 1(a), i.e., the probabilities of transition to a specific DS_i state. Specifically, in the first row, the probabilities of permanence in DS_0 given DS_0, i.e., $\mathbb{P}_{00}$, is defined as $\mathbb{P}\left(DS = DS_0 | DS_0, IM\right) = \mathbf{1} - \mathbb{P}_{01} - \mathbb{P}_{02}$. Here, particular attention is paid to the definition of $\mathbb{P}_{01}$, as also highlighted in the Figure by the * character. Indeed, the $\mathbb{P}_{01}$ is defined as the transition probabilities to attain DS_1 only. This is different than the probabilities of exceedance DS_1, which implies the probabilities of attaining DS_1 or worse, e.g., DS_2, as reported for completeness and clarity in Figure B.1 of the B. The transition diagrams below each fragility clarify this by remarking only the allowable transitions. Similarly, $\mathbb{P}_{02}$ is defined as the probability of reaching DS_2. There are no other worse conditions, since DS_2 stands for the collapse case. Note a straightforward definition for the second row, since only two states are allowed. Particularly, in this row, an $\boldsymbol{x}$ marks the transition state associated with recovery processes, not addressed in this paper. Finally, the last row of Figure 1(a) is not included because represents the absorption case, i.e., the unit probability of collapse given collapse as initial conditions. Moreover, Figure 8 reveals a greater dispersion in the '0-2' curves with respect to the others. This is strictly related to the lower number of clustered data in this transition state. Indeed, the dispersion of fragilities is positively related to the number of clustered data that describes the fragilities functions.

3.3.2 Surrogate-based MCS for state-dependent fragility functions

To test the methodology of Section 2, surrogate models are developed for the MDoF model, using as input the low dimensional representation of the seismic input, that is $\widehat{\mathbf{IM}}$. Specifically, PCE is adopted, since it provides a functional approximation of the computational model $\mathcal{M}(\widehat{\mathbf{IM}})$ through its spectral representation on suitably built basis $\psi_\alpha(\cdot)$ of polynomial functions Marelli et al. (2022). In real-world problems, due to limited computing power, the bases are truncated and the governing equation becomes:

$$\mathcal{Y} \approx \mathcal{M}^{PCE}\left(\widehat{\mathbf{IM}}\right) = \sum_{\alpha \in \mathcal{A}} c_\alpha \psi_\alpha\left(\widehat{\mathbf{IM}}\right), \tag{9}$$

where $\mathcal{A}$ is the set of selected multi-indices of multivariate polynomials and c_α are the corresponding coefficients to be determined. The c_α coefficients can then be calculated via projection,

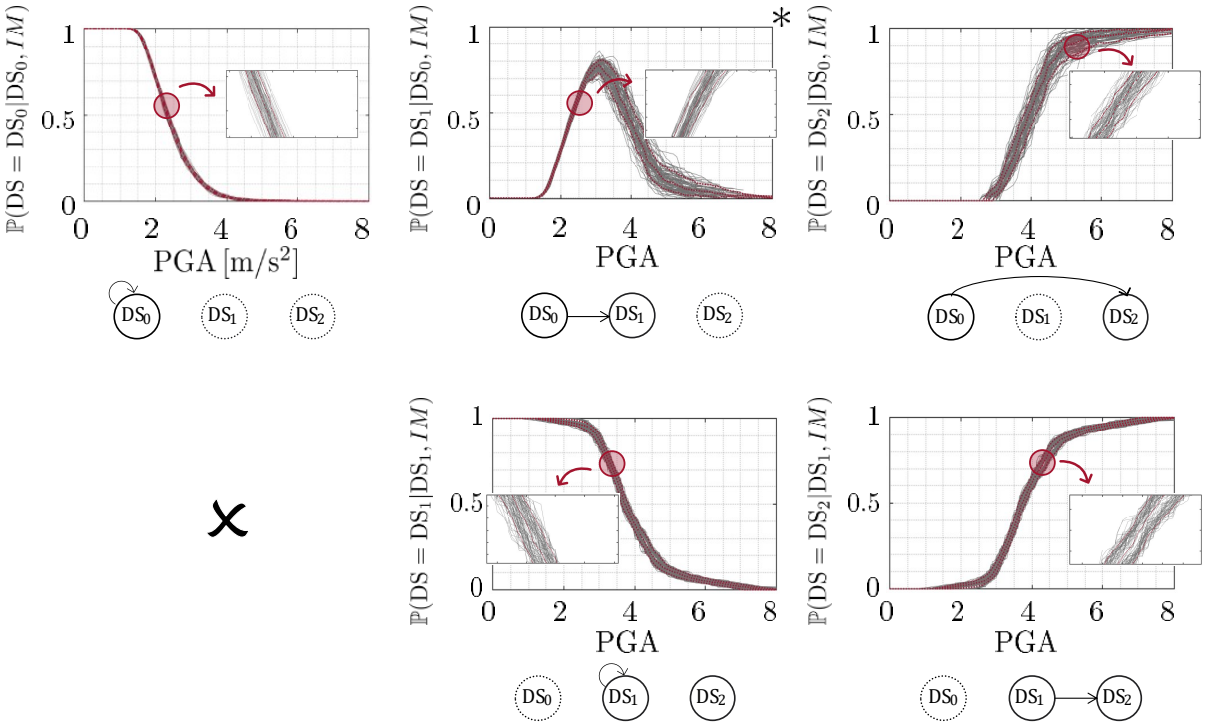

Figure 8: Brute-force MCS state-dependent fragility functions, by means of PGA: grey lines represent single seed simulations; dashed-dot dark-red lines depict the 99% confidence bounds, whilst dashed-dark red ones the 50%. PGA is the IM adopted, according to the global optimal $\beta_{\text{eff,glob}}$ among transition states. Notice that this Figure is in accordance with Eq. 1; therefore, the subplot at line 1 column 2 represents $\mathbb{P}(\mathrm{DS} = \mathrm{DS}_1|\mathrm{DS}_0, IM)$. Therefore, this is not a commonly used "fragility function," which reports the exceedance probability, i.e. $\mathbb{P}(\mathrm{DS} \geq \mathrm{DS}_1|\mathrm{DS}_0, IM)$. Figure B.1, in B, reports the commonly used fragility function.

i.e., Gaussian or sparse quadrature, or regression methods, i.e., least-square algorithms. In this framework, we adopted the least-square method to determine the coefficients. Specifically, separated c_α were estimated for each DoE $\mathcal{D}_s$, constituted by the clustered pairs of pseudo-IMs and QoI of FE model response, i.e., $(\widehat{\mathbf{IM}}; \mathcal{Y})$, as:

$$c_\alpha = \operatorname{argmin} \frac{1}{N} \sum_{i=1}^{N} \left[y_i - \sum_{\alpha \in \mathcal{A}} c_\alpha \psi_\alpha \left(\widehat{\mathbf{IM}}_i \right) \right]^2, \tag{10}$$

where N is the cardinality of the $\mathcal{D}_s$, $s \in [\mathrm{DS}_0; \mathrm{DS}_1]$ denotes the initial damage state level of the DoE, and $\{y^{(1)}, \ldots, y^{(N)}\}$ the realizations of $\mathcal{Y}$. The choice of a least-square regression strategy is motivated by the possibility of adopting the bootstrap resampling method. This is particularly insightful when the size of the $\mathcal{D}_s$ is limited, since it allows the user to explore exhaustively the information on the variability of the dataset. This can be achieved by first generating a set of bootstrap-resampled experimental design pairs $(\widehat{\mathbf{IM}}^{(b)}, \mathcal{Y}^{(b)})$ and then, by calculating a corresponding set of coefficients $c_\alpha^{(b)}$. Therefore, the response of each bootstrap PCE can be evaluated, yielding a family of b surrogate models that can be interpreted as trajectories. As recently explored in Marelli and Sudret (2017), this process of bootstrap-based

trajectories resampling can be directly employed to assess the confidence bounds on surrogate-based estimators.

In this case, surrogates are developed for the two sets of initial damage state conditions, i.e., DS_0 (pristine) and DS_1 (damaged) configurations. As recommended in Lüthen et al. (2021), the subspace pursuit (SP) solver was deployed in the PCE metamodel. Nevertheless, to identify the most suitable way to calculate the coefficients c_α of the PCEs, investigations were carried out on different sizes of the $\mathcal{D}_s$ and the vector of pseudo $\widehat{\mathbf{IM}}$, describing the seismic input. Specifically, the vector of pseudo $\widehat{\mathbf{IM}}$ is defined as the n, PCA most significant PCA principal components.

$$\widehat{\mathbf{IM}} = [\mathrm{PC}_1, \mathrm{PC}_2, \ldots, \mathrm{PC}_{n,PCA}]^T . \tag{11}$$

Figure 9 reports the variability covered by increasing the number of PCs through a scree plot. As one can notice, the first 3 PCs are sufficient to describe more than the 80% of the input data, 6 PCs the 90% and 10 PCs are needed to get the 99% of the input variance. Since there is no notable increase in computational burden between choosing either 6 or 10 PCs, we opt for the latter.

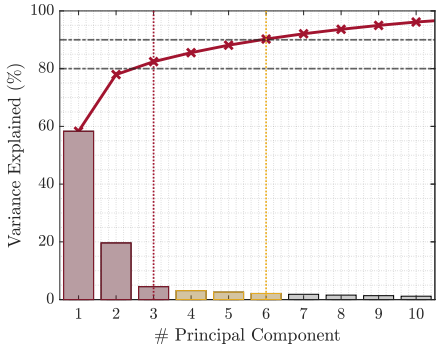

Figure 9: Scree plot of the seismic input.

To highlight which and how each im_i contributes to PCs, the first three PCs are displayed on the biplots in Figure 10. Particularly, in Figure 10, only the relevant IMs—i.e., the ones that present high scores—are plotted and labelled with the corresponding number ID of Table 1. Therefore, the information provided is twofold: (i) on the correlation among IMs; (ii) on the magnitude of the importance of the IMs in the definition of PCs. For instance, for PC_2: almost all the plotted IMs are positively correlated with PC_2 itself. The 33-IM, i.e.,$\mathrm{F_m}$, represent the exception, since it is in the opposite direction with PC_2, thus entailing a negative association. The positive/negative correlations and the order of magnitude are summarized in the coordinates of the PCs next to the biplot, until the tenth coefficient. More details on the correlations among IMs are discussed in the attached A, along with histograms and inferred marginal distributions. To determine the optimal size of the DoE, three measures of errors on the performances of the PCE surrogates were used: (i) the relative generalization ε_{gen}; (ii) the leave-one-out ε_{LOO}; and

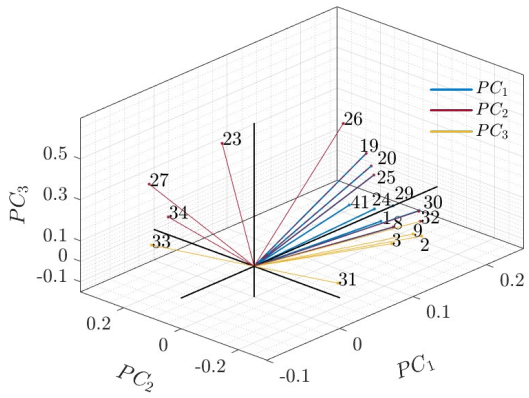

$$
\begin{aligned}
PC_1 = &+0.202\,\mathrm{ASI} + 0.198\,\mathrm{EPA} + 0.190\,\mathrm{E\text{-}ASA_{R_{200}}} + \\
&+0.190\,\mathrm{I_{CM}} + 0.186\,\mathrm{E_{cum}} + 0.183\,\mathrm{PGA} + \\
&+0.180\,\mathrm{I_A} + 0.175\,\mathrm{S_v(T_5)} + 0.175\,\mathrm{S_d(T_5)} + \ldots \\
PC_2 = &-0.021\mathrm{F_m} + 0.005\,\mathrm{AV} - 0.047\,\mathrm{I_{CM}} + 0.136\,\mathrm{S_v(T_1)} + \\
&+0.136\,\mathrm{S_a(T_1)} + 0.136\,\mathrm{S_d(T_1)}) + 0.109\,\mathrm{PGD} + \\
&+0.146\,\mathrm{I_{RG,v}} + 0.150\,\mathrm{PGV} + 0.149\,\mathrm{I_F} + \ldots \\
PC_3 = &-0.036\,\mathrm{T_d} + 0.149\,\mathrm{CAV} - 0.047\,\mathrm{I_{CM}} + -0.061\mathrm{F_m} + \\
&+0.180\,\mathrm{I_A} + 0.187\,\mathrm{E_{cum}} + 0.146\,\mathrm{I_{RG,v}} + 0.190\,\mathrm{I_c} + \\
&+0.149\,\mathrm{I_F} + 0.181\,\mathrm{S_d(T_5)} + \ldots
\end{aligned}
$$

Figure 10: 3D biplots of PCs 1, 2 and 3 for the IMs. For clarity, only the relevant im_i, identified by numbers as labelled in Table 1, are depicted.

(iii) the empirical ε_{emp} error. In particular, the former

$$\varepsilon_{gen} = \mathbb{E}\left[\left(\mathcal{Y} - \mathcal{M}^{PCE}\left(\widehat{\mathbf{IM}}\right)\right)^2\right] / \mathrm{Var}[\mathcal{Y}] \tag{12}$$

is best suited if a validation set is available; otherwise, as it is commonly the case with expensive computational models, the other two are preferred and evaluated with the following definition:

$$\varepsilon_{LOO} = \frac{\sum_{i=1}^{N_{sims}} \left(\boldsymbol{y}_i - \mathcal{M}^{PCE\setminus i}\left(\widehat{\boldsymbol{im}_i}\right)\right)^2}{\sum_{i=1}^{N_{sims}} \left(\boldsymbol{y}_i - \hat{\mu}_Y\right)^2}, \tag{13}$$

$$\varepsilon_{emp} = \frac{\sum_{i=1}^{N_{sims}} \left(\boldsymbol{y}_i - \mathcal{M}^{PCE}\left(\widehat{\boldsymbol{im}_i}\right)\right)^2}{\sum_{i=1}^{N_{sims}} \left(\boldsymbol{y}_i - \hat{\mu}_Y\right)^2}, \tag{14}$$

where N_{sims} is the total number of PCE-based MCS, y_i the realizations of $\mathcal{Y}$, and $\hat{\mu}_Y$ is the sample mean of the DoE response. In addition, the bootstrap technique is applied to PCE to provide a local error estimator. Precisely, resampling with substitution is used on the DoE $\mathcal{D}_s$, thus generating a set $B = 500$ bootstrap replications with the same number of sample points as the original $\mathcal{D}_s$. Each $b \in [1, B]$ replication is used to evaluate the corresponding PCE, yielding to b different sets of the PCE coefficients and predictions. Those b sets of responses are used to calculate the local variance and quantiles of the PCE predictor, exploiting all the information of the finite $\mathcal{D}_s$ size. Figure 11 shows the error trends against the DoE $\mathcal{D}_s$ size. The results agree with the latest investigations reported in Lüthen et al. (2021) concerning the ideal size of the DoE. Both the PCE-surrogate models for the $\mathcal{D}_0$ and $\mathcal{D}_1$ locate the optimal solution in 250 samples

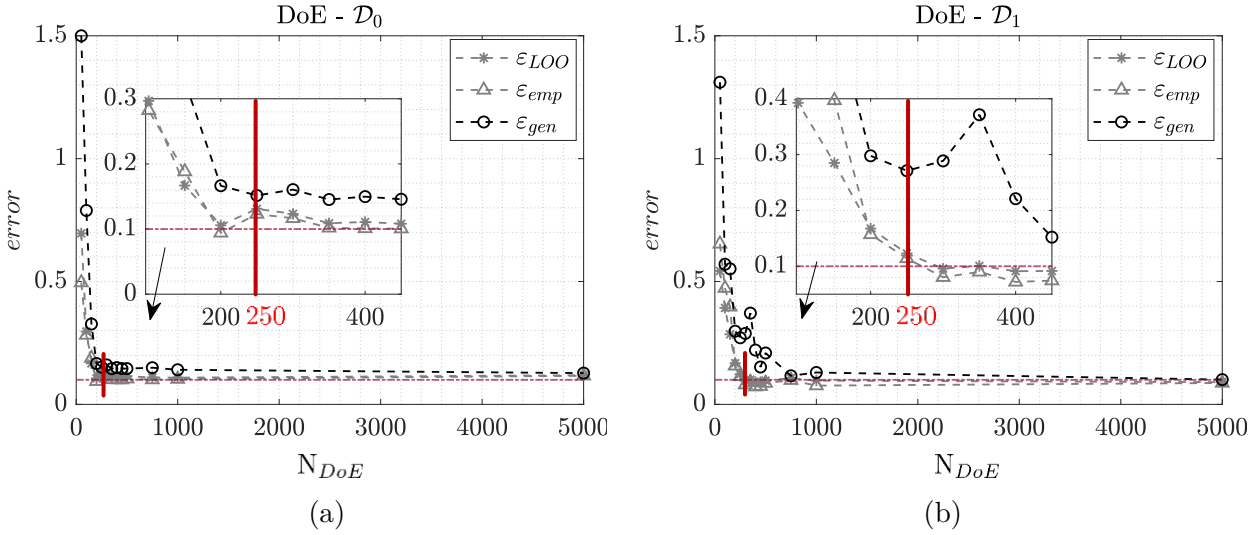

Figure 11: Error plots for the initial damage limit state (a) DS_0, namely DoE $\mathcal{D}_0$, and the (b) DS_1, namely DoE $\mathcal{D}_1$. The error threshold is fixed to 0.10 and is represented by the red dotted horizontal line. In both datasets, the ε_{LOO} and ε_{emp} perform better than the ε_{gen}, despite the vast validation set available in DoE $\mathcal{D}_1$, see Table 5a.

for the DoE dimension. Beyond this threshold, additional efforts to reduce model error result in marginal improvements or overfitting issues. The estimation of the PCE coefficients for the undamaged $\mathcal{D}_0$ initial condition converged to a polynomial degree 3 with $\varepsilon_{LOO} \simeq 0.15$. Figure 12 reports the histograms and validation $\mathcal{Y}_{\mathcal{D}_0}$-$\mathcal{Y}_{\text{PCE}}$ plots. A validation set of 10^4 samples is deployed, thanks to the large number of simulations carried out on the MDoF. A good agreement in terms of matching distributions between $\mathcal{Y}_{\mathcal{D}_0}$-$\mathcal{Y}_{\text{PCE}}$ is reached; also, samples-pairs are neatly aligned on the 45° line of the $\mathcal{Y}_{\mathcal{D}_0}$-$\mathcal{Y}_{\text{PCE}}$ plot, indicating a favourable performance. Similarly, for the damaged $\mathcal{D}_1$ initial condition of the system, the estimation of the PCE coefficients converged to a polynomial degree 3 with $\varepsilon_{LOO} \simeq 0.14$. Figure 13 displays histograms of 10^4 samples for the $\mathcal{Y}_{PCE}$ and FE $\mathcal{Y}_{\mathcal{D}_1}$ data. Again, since $\mathcal{Y}_{\mathcal{D}_1}$-$\mathcal{Y}_{\text{PCE}}$ pairs are well aligned to the 45° line, a good agreement is demonstrated. Finally, state-dependent fragility curves are evaluated based on the results provided by the bootstrap PCE of both the pristine-$\mathcal{D}_0$ and the damaged-$\mathcal{D}_1$ datasets. As for the results of the brute-force MCS, fragilities are displayed referring to the optimal global IM. Thus, the $\beta_{\text{eff,glob}}(IM_i)$ of Eq. 8 is evaluated for each transition state over the i to 41 IMs. Next, the global optimal IM^{**} is selected as follow $IM^{**} = \text{argmin}_{IM_i}\ \beta_{\text{eff,glob}}(IM_i)$. Thus, Figure 14 shows the state-dependent fragilities as functions of the global optimal IM^{**}, i.e., the PGA.

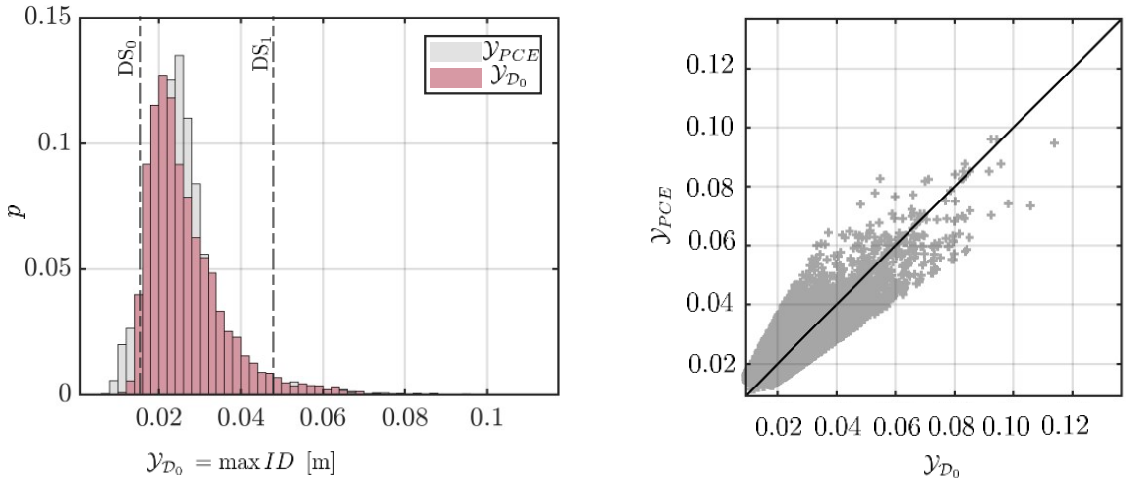

(a) (b)

Figure 12: (a) Comparison of the histograms for the outputs, $\mathcal{Y}_{PCE}$, of the PCE metamodel and the EDPs, $\mathcal{Y}_{\mathcal{D}_0}$, of the $\mathcal{D}_0$ dataset, i.e., the initial damage state condition DS_0, and (b) the associated validation $\mathcal{Y}_{\mathcal{D}_0}$-$\mathcal{Y}_{\mathrm{PCE}}$ plot.

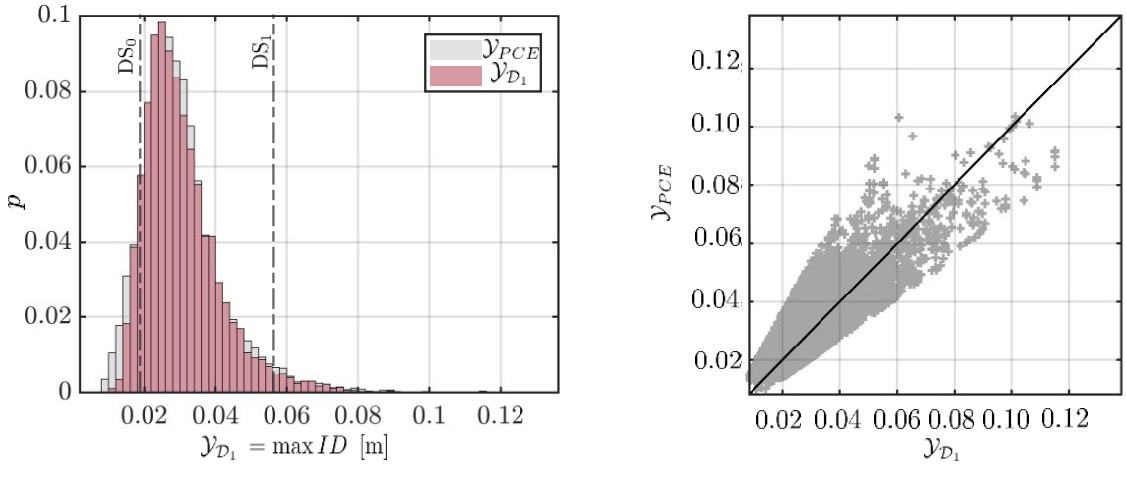

(a) (b)

Figure 13: (a) Comparison of the histograms for the outputs, $\mathcal{Y}_{PCE}$, of the PCE metamodel and the EDPs, $\mathcal{Y}_{\mathcal{D}_1}$, of the $\mathcal{D}_1$ dataset, i.e., the initial damage state condition DS_1, and (b) the associated validation $\mathcal{Y}_{\mathcal{D}_1}$-$\mathcal{Y}_{\mathrm{PCE}}$ plot.

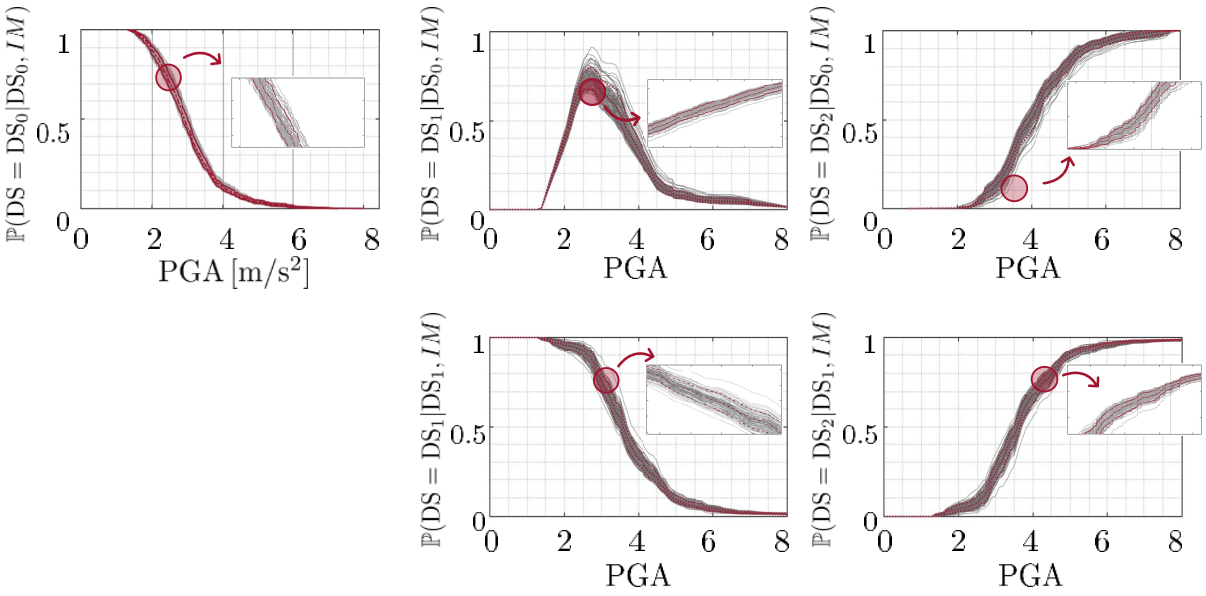

Figure 14: Bootstrap-PCE-based MCS state-dependent fragility functions: grey lines represent single seed simulations; dashed-dotted dark red lines depict the 90% confidence bounds, whilst dashed-dark red ones the 50%.

3.3.3 Validation of the framework

A visual comparison between state-dependent fragilities derived by brute-force MCS (benchmark case) and surrogate-based MCS shows a good agreement, see for instance Figure 8 vs Figure 14, respectively. From a quantitative point of view, we measure the difference between the two fragility functions using the efficiency indices, the Kullback–Leibler (KL) divergence, and the Kolmogorov-Smirnov (KS) distance[2]. In particular, Table 6 gathers the $\Delta(\beta_{\text{eff}})$ expressed as $\left(|\beta_{\text{eff}}^{\text{PCE}} - \beta_{\text{eff}}|\right)/\beta_{\text{eff}}$ for each of the best indices of the transition states. The closer the delta is to 0, the better the matching of surrogate-based MCS with brute-force MCS results. It is generally observed that the $\Delta(\beta_{\text{eff}})$ remains under the 0.20 threshold, which we consider, in this case, a good matching of responses. The KL divergence, $D_{\text{KL}}(P \parallel Q)$, quantifies how one probability

Table 6: $\Delta(\beta_{\text{eff}})$ efficiency indices calculated as $\left(|\beta_{\text{eff}}^{\text{PCE}} - \beta_{\text{eff}}|\right)/\beta_{\text{eff}}$ for the same top IMs for each transition states.

Frag. '0-0' Optimal IM	**$\Delta(\beta_{\text{eff}})$ index**	**Frag. '0-1' Optimal IM**	**$\Delta(\beta_{\text{eff}})$ index**	**Frag. '0-2' Optimal IM**	**$\Delta(\beta_{\text{eff}})$ index**	**Frag. '1-1' Optimal IM**	**$\Delta(\beta_{\text{eff}})$ index**	**Frag. '1-2' Optimal IM**	**$\Delta(\beta_{\text{eff}})$ index**
PGA	0.12	$I_{RG,a}$	0.13	ASI	0.14	ASI	-0.17	E – ASA_{R80}	0.07
IC	0.15	PGA	0.14	EPA	0.13	EPA	-0.19	E-ASA_{R200}	0.08
$I_{RG,a}$	0.15	$I_{RG,v}$	0.16	RMS(ü)	0.15	PGA	-0.19	E-ASA_{R100}	0.08
E-ASA_{R200}	0.12	E-ASA_{R200}	0.16	PGA	0.14	$I_{RG,v}$	-0.17	E-ASA_{R150}	-0.08
RMS(ü)	-0.05	PGD	0.16	E-ASA_{R200}	0.15	$I_{RG,a}$	-0.15	$I_{RG,a}$	-0.16

distribution P is different from a second Q, defined on the same sample space. Specifically, P denotes the empirical probability distribution (Figure 14); while Q represents the empirical probability distribution of the mean brute-force MCS state-dependent fragillities (Figure 8). Thus, KL is evaluated as provided in Eq. 15:

$$D_{\text{KL}}(P \parallel Q) = \sum_{x \in \mathcal{X}} P(x) \ \log\left(\frac{P(x)}{Q(x)}\right) \tag{15}$$

where $\mathcal{X}$ represents the sample space, that is, the domain of the optimal IM for each transition state. Figure 15 shows the mean PCE-based and brute-force MCS state-dependent fragility functions for the transition states '0-1', '0-2', and '1-2'. As Table 7 shows, the D_{KL} distance is bounded $\in [0.12 - 0.19]$, meaning an overall good agreement (see Perez-Cruz (2008)). The KS distance is defined as

$$D_{\text{KS}} = \sup_x |F_1(x) - F_2(x)|, \tag{16}$$

where F_1 and F_2 are the mean empirical cumulative distribution functions of the MCS brute-force and surrogate-based fragilities, respectively, and sup is the supremum function. Thus, Table 7 collects the results. The distance between the mean of the MCS brute-force functions and the

[2]Technically speaking, the fragility functions are not proper CDFs, as the variable IM is in its conditional form. However, as they are assumed to be monotonically increasing, then they can be treated as CDFs, and the KL and KS distances are therefore used to assess the difference between the MCS and the PCE-based fragilities.

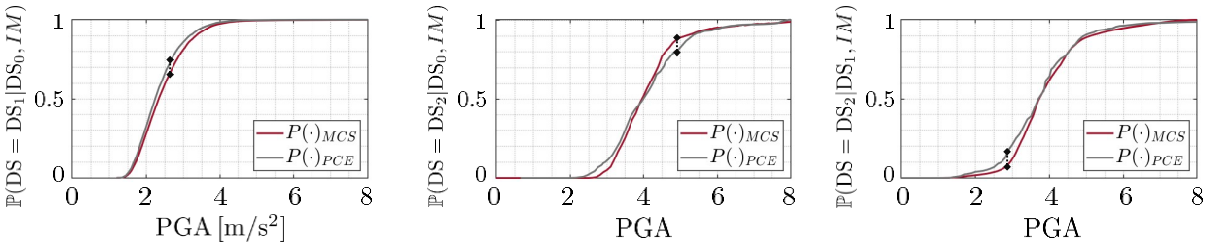

Figure 15: Mean PCE-based and brute-force MCS fragility functions comparisons for the transition states '0-1', '0-2', and '1-2'with PGA as IM. Note that the probability of exceedance is adopted for the transition state '0-1'.

surrogate-based is considered acceptable within the simulation framework. Moreover, fragilities must be integrated with the hazard curves; therefore, we consider these minimal differences as negligible.

Table 7: D_{KS} and D_{KL} measures for the mean PCE-based *vs* brute-force MCS state-dependent fragility functions.

	IM = PGA		
	'0-1'	**'0-2'**	**'1-2'**
D_{KS}	0.067	0.085	0.096
D_{KL}	0.164	0.200	0.186

4 Industrial case: vertical tank installed on a 3D braced-frame structure

The above framework was applied to the SPIF #2 case study, Quinci et al. (2023),Nardin et al. (2022),Butenweg, C. et al (2020). Specifically, the object of the state-dependent fragility analysis was the vertical tank installed on the steel-BF industrial substructure.

4.1 Step $\mathcal{A}$ - Computational model description

4.1.1 FE physics-based model

We consider the FE model developed for the SPIF #2 experimental research campaign. Figure 16(a) shows the industrial substructure model tested on the shaking table. The mock-up consists of a full-scale 3-storey steel BF structure with flexible floors. Several NSCs of the industrial process were installed, like tanks, cabinets, bolted flange joints, and T-joints. Particularly, the complex dynamic interaction between the main steel structure and one of the NSCs—the vertical tanks mounted on the first level—was examined. The strong displacement

exhibited by those components deserved attention. This is because their damage can lead to severe consequences. Figure 16(a) shows the investigated vertical tank. Figure 16(b) reports a detail of the *ad-hoc* designed stick model for the tanks and its expensive reference high-fidelity local FE model. The stick model was developed with the goal to: (i) mimic the modal properties and (ii) catch the different effects of the participating seismic mass on the supporting girders system. The latter is particularly delicate since the participating mass varies with the intensity level of the seismic excitation. A thorough discussion on FE modelling and calibration of the global SPIF #2 model of Figure 16(c) is reported in Quinci et al. (2023). The shake table

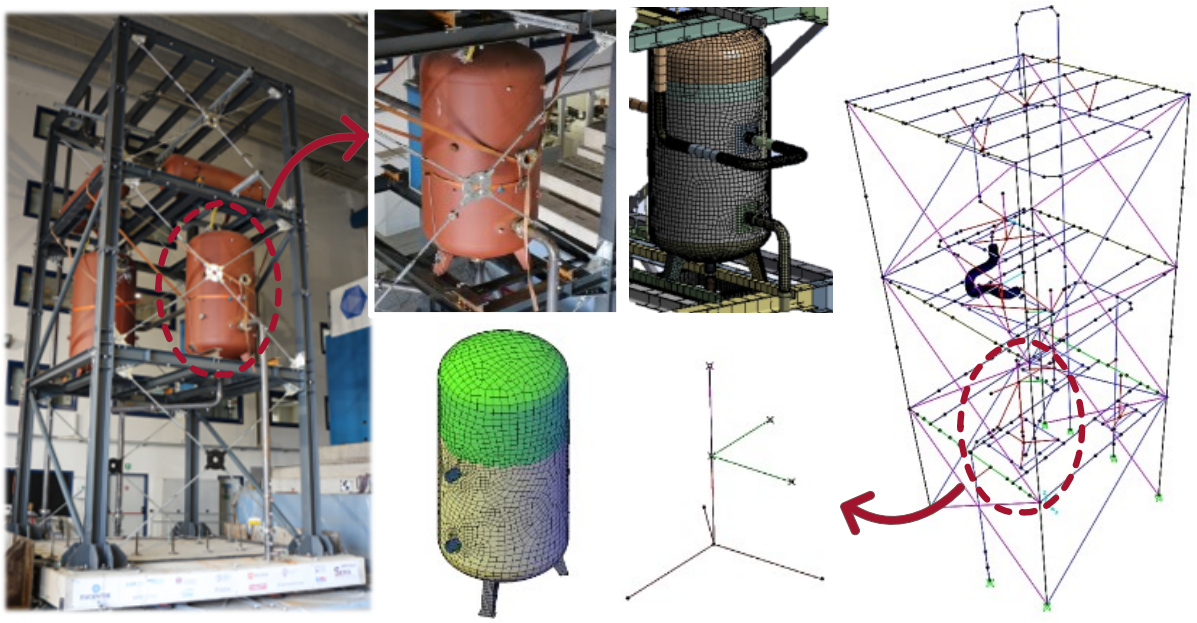

Figure 16: The SPIF #2 mock-up: (a) photo of the braced frame (BF) configuration on the shake table of EUCENTRE Facilities and details of the vertical tank installed at the first level; (b) SAP2000®high-fidelity local FE model and *ad-hoc* implemented stick-model for the vertical tank; (c) global SAP2000®FE model of SPIF #2.

tests showed that the vertical tanks were one of the most critical elements among the installed components. Therefore, we developed fragility analysis for these elements, using the bootstrap PCE technique of the previous Section.

4.2 Step $\mathcal{B}$ - Input definition

The framework outlined in Section 2 is adopted. Sequences of seismic events were assigned to the FE model of SPIF #2 to (i) simulate different damage initial configurations and (ii) cover each transition state. A total of 100 gms sequences, consisting of chains of 5 earthquakes each, were implemented by the same ensemble of gms generated by the GMM of Subsection 3.2. The computational cost pro single sequential NLTHA is ∼30 min on an Intel(R) Core(TM) i9-10900K

CPU @3.70GHz, 10 Core(s) - 128 GB RAM. Both the number of gms in a single sequence and the total number of sequential NLTHAs were determined by a trade-off between the total time required for analysis and a well-defined population of the transition matrix of Figure 1(a). The transition matrix for the vertical tank was defined on two performance limit states, e.g., DS_1 and DS_2. Those were set according to literature recommendations, see Vathi et al. (2017), and confirmed by the experimental campaign, see Quinci et al. (2023). The first, DS_1, is the design basis earthquake (DBE), which is linked to the operation and functionality of the process plant. The second, DS_2, is the safe shutdown earthquake (SSE) limit state, for which the fundamental safety functions can be ensured with minor damages, although the facility is no longer operational. Thresholds were experimentally identified by maximum acceleration values recorded at the base of the vertical tank

$$\max|\ddot{u}_{base}^{v.tank}| = \begin{cases} 10\,\mathrm{m/s^2}, & \mathrm{DBE}\,(\mathrm{DS}_1) \\ 16\,\mathrm{m/s^2}, & \mathrm{SSE}\,(\mathrm{DS}_2) \end{cases} \tag{17}$$

for the DBE and SSE, respectively, as reported in Quinci et al. (2023).

4.3 Step $\mathcal{C}$ - QoI response

4.3.1 NLTHAs and experimental design generation

As illustrated in Figure 2, the results of the NLTHAs performed on the FE model were clustered into the transition states of Figure 1(a). Specifically, $\mathcal{D}_0$ indicates the dataset associated with pristine initial damage conditions, whilst $\mathcal{D}_1$ denotes the dataset for which the threshold associated with the DBE limit state was exceeded. Lastly, $\mathcal{D}_2$ collects the results of simulations for which the SSE limit state was attained. As Table 17 shows, almost 47% of the simulations belong to the $\mathcal{D}_0$ damage state initial condition. Particularly, 13% and 7% transitioned from undamaged initial conditions to exceeding the DBE and SSE threshold at the end of the NLTHAs, respectively. Instead, 38% of simulations belong to $\mathcal{D}_1$, out of which 16% stayed in the same damage level even after other seismic shocks. Finally, 15% of the simulations reached the absorption state. Again, the 41 IMs of Table 1 were evaluated for each gms of the NLTHA simulations. PCA was then applied to reduce the order of the input dimension. Specifically, 10 PCs were used to cover 99% of the variability of data.

4.3.2 PCE metamodelling

State-dependent fragilities required many more analyses than the ones performed on the expensive-to-run FE model. Hence, two metamodels were implemented to overcome the computational and time issues. Specifically, the first metamodel was built on the experimental design $\mathcal{D}_0$ of simulations belonging to the pristine initial condition dataset. The second on the DoE $\mathcal{D}_1$, the family of simulations with initial conditions attaining the DBE limit state. Resampling with substitution was used on both the experimental design $\mathcal{D}_{0,1}$, thus generating sets of bootstrap

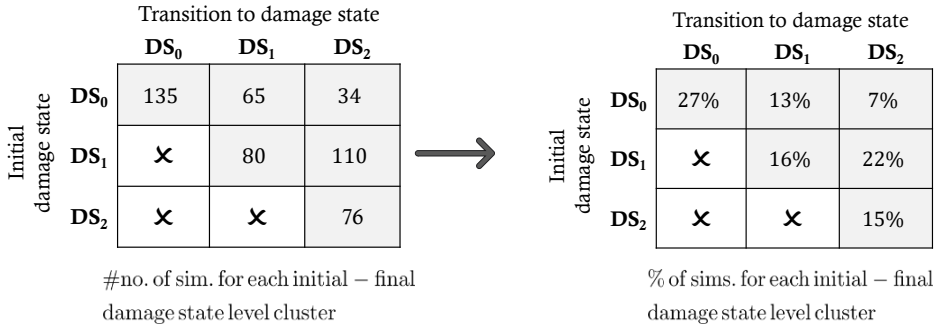

(a) (b)

Figure 17: Transition state matrices for the SPIF #2: (a) counters and (b) percentages of simulation for each initial-final damage state level cluster, respectively.

replications to estimate confidence bounds. Specifically, bootstrap PCE was carried out with a q-norm truncation of $q = 0.50$, maximum allowed interaction $r = 2$ and a total number of replications $B = 500$. Based on the latest findings of Lüthen et al. (2021), the subspace pursuit (SP) solver was adopted with 10 PCs. As a result, Figure 18(a) reports the histogram of the surrogate predictor over the histogram distribution of the $\mathcal{D}_0$. The limit state thresholds of DBE and SSE are also reported. A favourable performance is attained, with a final ε_{LOO} error of 4.17E-02. The estimation of bootstrap PCE coefficients converged to a polynomial degree order of 3. Moreover, Figure 18(b) shows the control $\mathcal{Y}_{\mathcal{D}_0}$-$\mathcal{Y}_{PCE}$ plot: a good alignment is found with the 45° line, which represents the ideally perfect match between true and surrogate data. Similarly,

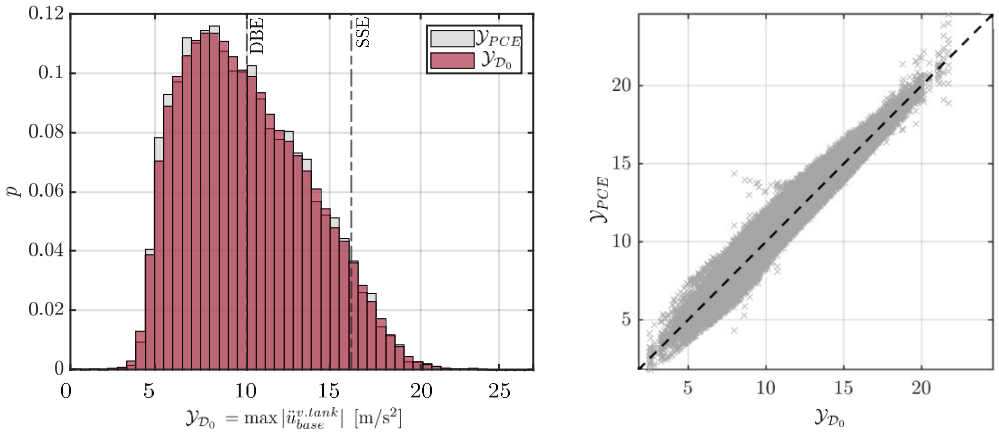

(a) (b)

Figure 18: (a) Histogram distribution of the PCE surrogate $\mathcal{Y}_{PCE}$ (light grey) predictor *vs* the $\mathcal{Y}_{\mathcal{D}_0}$ original data of the initial undamaged condition dataset; (b) control plot of the performance of the $\mathcal{Y}_{PCE}$ surrogate model *vs* the $\mathcal{Y}_{\mathcal{D}_0}$ reference experimental design samples.

bootstrap PCE was performed for the experimental design $\mathcal{D}_1$. Anew, a q-norm truncation $q = 0.50$, maximum allowed the interaction $r = 2$ and a number of replications $B = 500$ was

applied. As a result, Figure 19(a) reports the histogram distribution of both the $\mathcal{Y}_{PCE}$ predictor and the $\mathcal{Y}_{\mathcal{D}_1}$ data of the damaged initial state condition. A generally good agreement is found, with a few exceptions in the range between $[21-22] m/s^2$. This is reflected also in the control plot $\mathcal{Y}_{PCE}$-$\mathcal{Y}_{\mathcal{D}_1}$ of Figure 19(b), where the dispersion is greater in that range. The estimation of the PCE coefficients converged at a polynomial degree of order 5 with a final ε_{LOO} error of 4.73E-02.

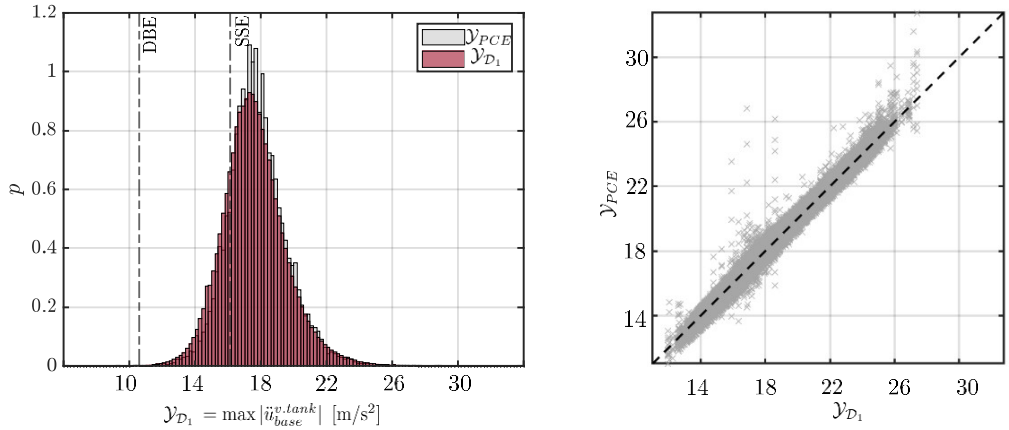

(a) (b)

Figure 19: (a) Histogram distribution of the PCE surrogate $\mathcal{Y}_{PCE}$ (light grey) predictor *vs* the $\mathcal{Y}_{\mathcal{D}_1}$ original data of the initial undamaged condition dataset; (b) control plot of the performance of the $\mathcal{Y}_{PCE}$ surrogate model *vs* the $\mathcal{Y}_{\mathcal{D}_1}$ reference experimental design samples.

4.4 Fragility assessment

Following Section 3, a global optimal IM descriptor for the derivation of fragility functions is evaluated. Table 8 gathers the ranking of the first five minimum $\beta_{\text{eff,glob}}$ for the SPIF case study, derived by Eq. 8. It emerges that IMs strictly correlated with acceleration or energy content are the most suitable for the case study. Next, we select PGA as the optimal IM and compute state-dependent fragilities using PCE-surrogate models as described in Section 2.

	Global Optimal IM	$\beta_{\text{eff,glob}}$ **index [%]**
1	PGA	4.02
2	E_{cum}	4.35
3	I_A	5.07
4	I_F	5.31
5	$I_{RG,a}$	7.42

Table 8: Ranking of the optimal IMs according to the global $\beta_{\text{eff,glob}}$, defined in Eqn. 8.

Figure 20 shows the probabilistic description of state-dependent fragilities as functions of the

PGA. The curves representing the 1%-50%-99% percentiles are displayed with black-dotted thick lines, whilst the 10%-90% with red-dotted lines, and their area with darker to lighter red-shaded colours. In C, we report the collection of state-dependent fragility functions based on the optimal β_{eff} index for each transition state in Figure C.1. Moreover, the commonly referred fragility functions as the probability of exceedance of a certain threshold, in this case, the DS_1 threshold given DS_0 initial damage condition, is reported in Figure C.2.

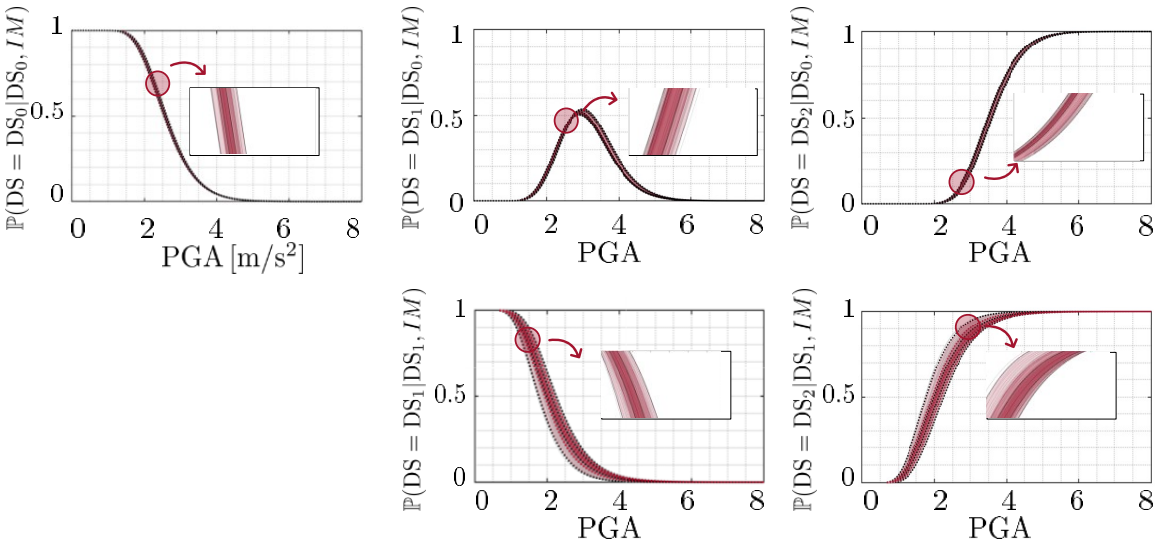

Figure 20: Bootstrap-PCE state-dependent fragility curves of the SPIF #2 vertical tank: black-dotted thick lines stand for the 1%, 50%, and 99% percentiles. Red-dotted lines for the 10% and 90% percentiles, along with their area with darker to lighter red-shaded colours.

5 Conclusions and Future developments

An innovative, non-intrusive UQ-based framework for assessing state-dependent fragility functions has been proposed. The framework builds on a stochastic representation of seismic sequences, calibrated and validated FE models, principal component analysis (PCA) representation of the input, and advanced polynomial chaos expansion (PCE)-based surrogate modelling. The proposed framework provides for both vast flexibility and integration with FEM experts as well as extreme computational efficiency. State-dependent fragility analysis requires a vast number of NLTHAs, based on time series of stochastic seismic sequences. However, when considering realistic computational models, the significant computing demands of an extensive set of sequential NLTHAs generally hinder this direct derivation of state-dependent fragilities. Hence, we propose an innovative UQ-based framework that combines a PCA representation of the stochastic input and an advanced PCE surrogate modelling of the QoI of the system. Specifically, we first performed a reduced number of stochastic seismic sequence NLTHAs on expensive-to-run FEM. Next, the resulting QoIs were clustered according to predefined damage initial states. At the same time, we performed PCA on the exhaustive vector of $\boldsymbol{IM}$, to obtain a low-dimensional

input representation of the time series sequences $\widehat{\boldsymbol{IM}}$. Next, on the pairs of clustered QoIs and the $\widehat{\boldsymbol{IM}}$—i.e., the DoE—, we built different PCE surrogate models, one for each initial damage state of the system. Successively, the vast number of MCS surrogate-based analyses enabled us to derive non-parametric state-dependent fragility functions. In particular, the UQ-based framework was applied twice. First, it was tested and validated on a simple yet realistic 2D MDoF system endowed with Bouc-Wen hysteresis. Specifically, given the inexpensive-to-run benchmark case study, state-dependent fragilities were evaluated both via the MCS brute-force method and the MCS PCE-based one. Global and local efficiency β_{eff} indeces for each transition states were evaluated to determine the optimal IM for fragility assessment. Moreover, qualitative and quantitative comparisons through $\Delta\beta_{\text{eff}}$ and statistical measures confirmed the acceptable performance of the developed framework. Second, the validated methodology was applied to derive seismic state-dependent fragility functions for an industrial process component. Specifically, the critical vertical tank of the 3-storey 3D BF industrial mock-up of project SPIF #2 was considered. Following the previous example, a given number of sequences of synthetic ground motions were assigned as input for NLTHAs on the refined FEM of the coupled SPIF system. Then, clustering of the QoIs along with PCA for dimensionality reduction of the stochastic seismic sequences of the input was performed. Next, PCE surrogate models were built for the identified initial damage state conditions. Moreover, MCS PCE-based state-dependent fragility functions were evaluated. Thus, the developed framework allows to unlock the possibility of efficiently computing state-dependent fragility for a variety of problems. In addition, the versatility of the framework allows us to extend it to a vector of IMs for fragility assessment, in the future. The use of the framework for aftershock sequences is being considered as a second future direction, provided with a stochastic representation of input sequences. Finally, either the single state-dependent fragility function or the entire framework can be used to estimate seismic risk.

Acknowledgements

The research leading to these results has received funding from (i) the European Community's "NextGeneration EU Programme" [PRIN − 2022MJ82MC_001 − CUPE53D23004440006] - for the first and the last author; (ii) the National Project MUR PNRR M4C2-CN1-SPOKE 9 - for the first and the third author; and (iii) the Italian Ministry of Education, University and Research (MIUR) in the frame of the "Departments of Excellence 2023-2027" (grant $L232/2016$) - for the third and the last author.

A - Histograms and distributions of the input.

Figure A.1 illustrates the correlation among the IM parameters, which varies $[-1, +1]$. It emerges:

- high correlations among E-$ASA_{R,x}$, Sa and E-$ASA_{R,x}$ as the frequency drop R_x increases - indexes from 36 to 41;
- significative correlations among IMs sensitive to acceleration EPA - idx. 30 - , ASA_{40} - idx. 28, and ASI - idx. 29;
- negative correlations or low correlations for the significant time duration T_d - idx. 23, the Cosenza-Manfredi intensity I_{CM} - idx. 27 - and both the frequency-related IMs mean F_m - idx. 33 - and rate of change mean frequencies $\dot{F}_m$ - idx. 34;
- linear correlations between Sa-Sv and Sv-Sd - idxs. 4-18, as expected by the definitions.

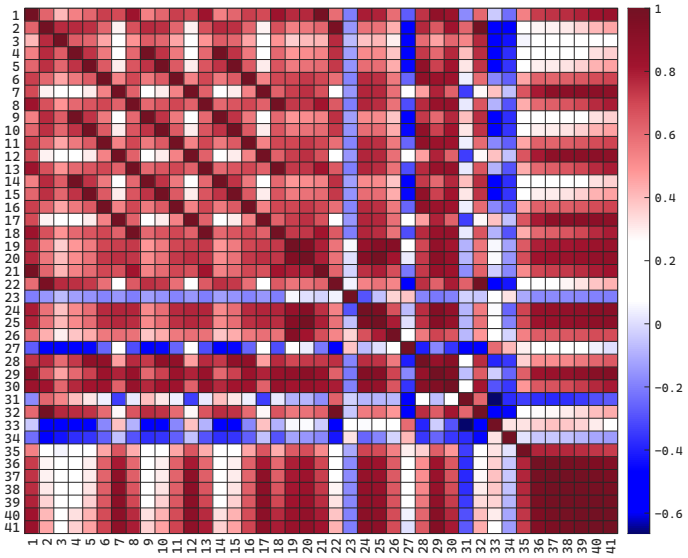

Figure A.1: Correlation map between input IM parameters.

Table 9 and Figures A.2-A.6 gather the histograms and inferred *pdf* for each IM presented in Table 1 of Section 3.2.

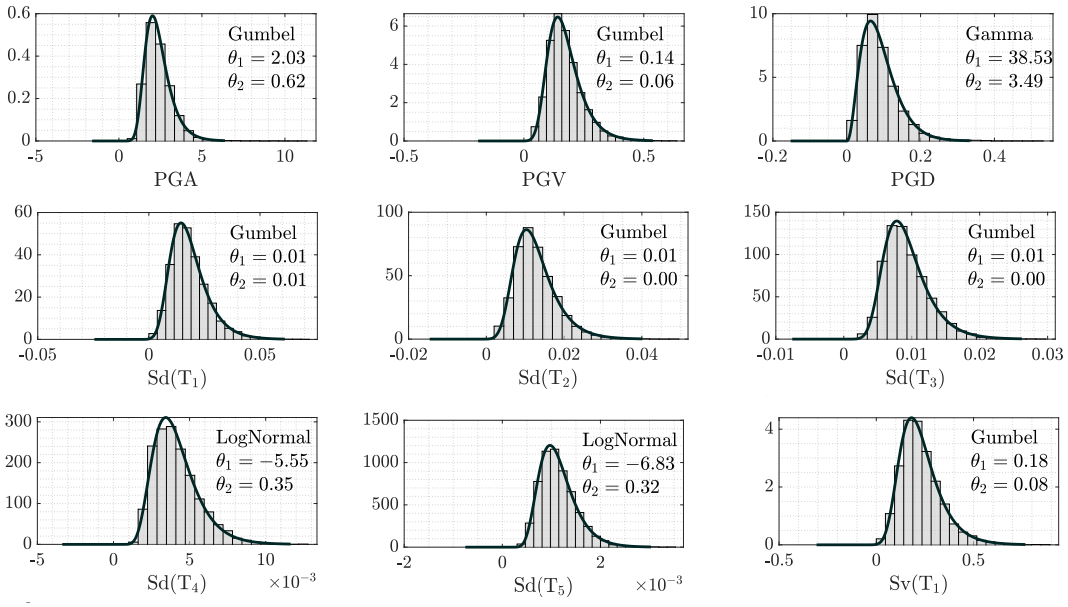

Figure A.2: Histograms and distributional models for IMs from 1 to 9.

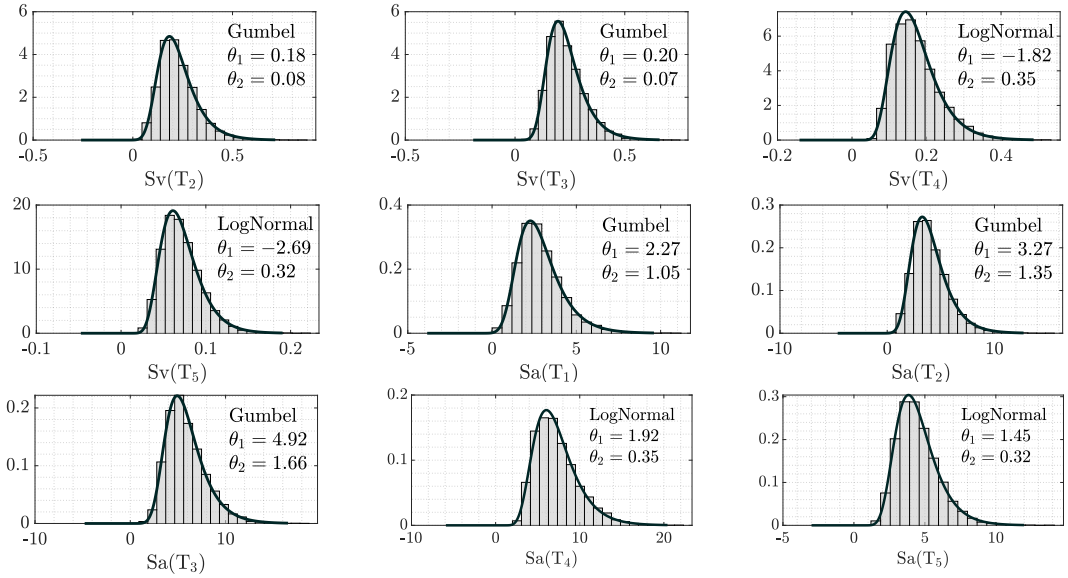

Figure A.3: Histograms and distributional models for IMs from 10 to 18.

Table 9: Histograms and distributional models inferred for each IM.

Index	Name	Type	Parameters	Moments
1	PGA	Gumbel	2.027e+00, 6.236e-01	2.387e+00, 7.998e-01
2	PGV	Gumbel	1.408e-01, 5.683e-02	1.736e-01, 7.289e-02
3	PGD	Gamma	3.853e+01, 3.489e+00	9.055e-02, 4.848e-02
4	$Sd(T_1)$	Gumbel	1.447e-02, 6.679e-03	1.833e-02, 8.566e-03
5	$Sd(T_2)$	Gumbel	1.031e-02, 4.263e-03	1.277e-02, 5.468e-03
6	$Sd(T_3)$	Gumbel	7.792e-03, 2.635e-03	9.313e-03, 3.379e-03
7	$Sd(T_4)$	LogNormal	-5.551e+00, 3.517e-01	4.133e-03, 1.500e-03
8	$Sv(T_5)$	LogNormal	-6.831e+00, 3.239e-01	1.137e-03, 3.782e-04
9	$Sv(T_1)$	Gumbel	1.814e-01, 8.370e-02	2.297e-01, 1.074e-01
10	$Sv(T_2)$	Gumbel	1.835e-01, 7.591e-02	2.274e-01, 9.736e-02
11	$Sv(T_3)$	Gumbel	1.958e-01, 6.622e-02	2.341e-01, 8.493e-02
12	$Sv(T_4)$	LogNormal	-1.815e+00, 3.517e-01	1.732e-01, 6.285e-02
13	$Sv(T_5)$	LogNormal	-2.690e+00, 3.239e-01	7.156e-02, 2.380e-02
14	$Sa(T_1)$	Gumbel	2.273e+00, 1.049e+00	2.878e+00, 1.345e+00
15	$Sa(T_2)$	Gumbel	3.268e+00, 1.352e+00	4.048e+00, 1.733e+00
16	$Sa(T_3)$	Gumbel	4.922e+00, 1.664e+00	5.883e+00, 2.134e+00
17	$Sa(T_4)$	LogNormal	1.920e+00, 3.517e-01	7.260e+00, 2.634e+00
18	$Sa(T_5)$	LogNormal	1.452e+00, 3.239e-01	4.502e+00, 1.497e+00
19	I_A	LogNormal	-6.729e-01, 5.712e-01	6.006e-01, 3.730e-01
20	E_{cum}	LogNormal	1.342e+00, 5.453e-01	4.439e+00, 2.612e+00
21	$I_{RG,a}$	Gumbel	4.151e+00, 1.222e+00	4.856e+00, 1.567e+00
22	$I_{RG,v}$	LogNormal	-5.098e-01, 2.745e-01	6.237e-01, 1.745e-01
23	T_d	Gaussian	8.696e+00, 1.637e+00	8.696e+00, 1.637e+00
24	RMS(ü(t))	LogNormal	-7.590e-01, 2.845e-01	4.875e-01, 1.415e-01
25	IC	LogNormal	-6.627e-02, 4.070e-01	1.017e+00, 4.315e-01
26	CAV	Gamma	9.262e-03, 9.638e+00	1.041e+03, 3.352e+02
27	I_{CM}	LogNormal	2.178e+00, 4.817e-01	9.915e+00, 5.067e+00
28	ASA_{40}	Gamma	1.122e-01, 8.580e+00	7.647e+01, 2.611e+01
29	ASI	LogNormal	6.025e+00, 2.910e-01	4.315e+02, 1.283e+02
30	EPA	Gamma	4.737e-02, 1.134e+01	2.393e+02, 7.108e+01
31	$I_{v/a}$	Gamma	1.343e+02, 9.941e+00	7.400e-02, 2.347e-02
32	I_F	Gumbel	2.407e-01, 9.524e-02	2.957e-01, 1.221e-01
33	F_m	Gaussian	4.649e+00, 4.801e-01	4.649e+00, 4.801e-01
34	$\dot{F}_m$	GumbelMin	-2.667e-04, 2.347e-04	-4.022e-04, 3.011e-04
35	FAS_{area}	Exponential	3362	2.974e-01, 2.974e-01
36	$E - ASA_{R_{40}}$	LogNormal	2.371e+00, 3.504e-01	1.138e+01, 4.115e+00
37	$E - ASA_{R_{67}}$	LogNormal	3.283e+00, 3.387e-01	2.823e+01, 9.842e+00
38	$E - ASA_{R_{80}}$	LogNormal	3.561e+00, 3.325e-01	3.719e+01, 1.271e+01
39	$E - ASA_{R_{100}}$	LogNormal	3.917e+00, 3.229e-01	5.296e+01, 1.756e+01
40	$E - ASA_{R_{150}}$	LogNormal	4.495e+00, 3.110e-01	9.398e+01, 2.995e+01
41	$E - ASA_{R_{200}}$	LogNormal	4.879e+00, 3.056e-01	1.378e+02, 4.313e+01

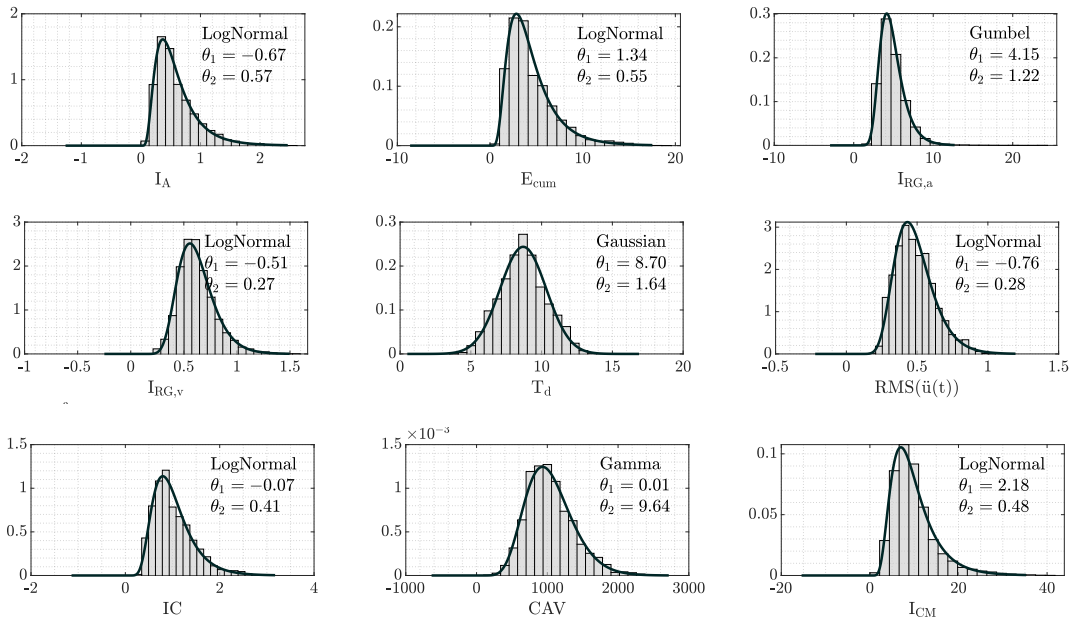

Figure A.4: Histograms and distributional models for IMs from 19 to 27.

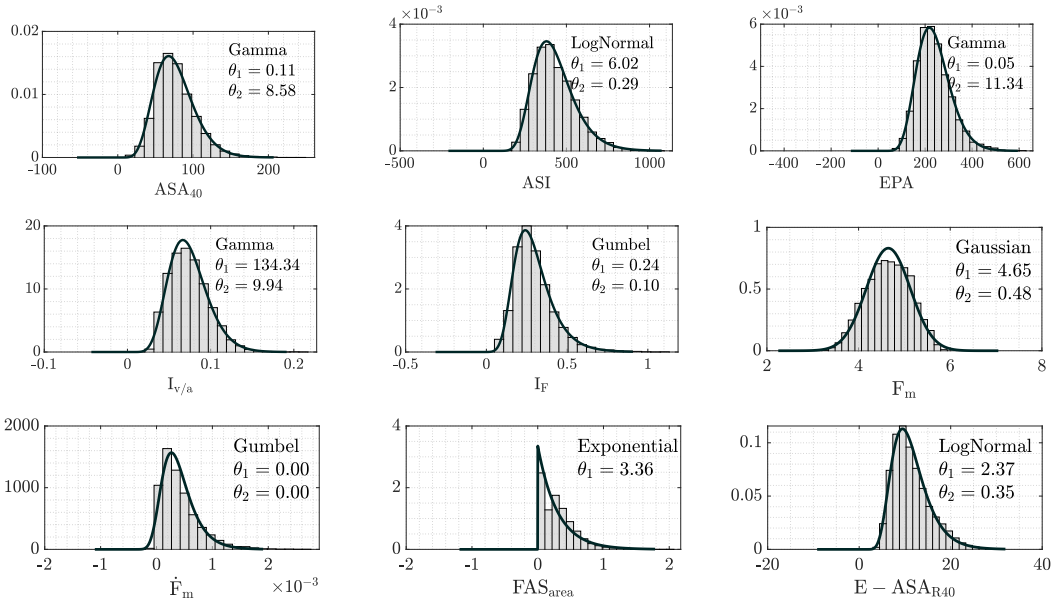

Figure A.5: Histograms and distributional models for IMs from 28 to 36.

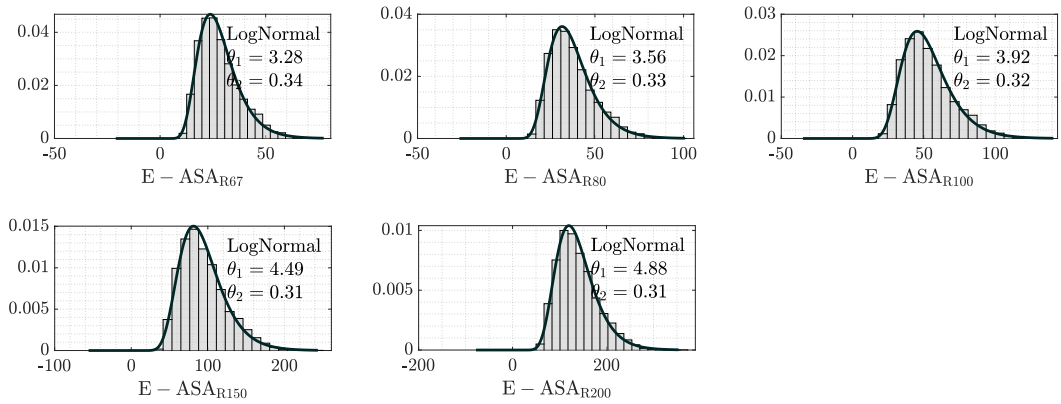

Figure A.6: Histograms and distributional models for IMs from 37 to 41.

B - MDoF support material

State-dependent fragility: $\mathbb{P}(\mathrm{DS} \geq \mathrm{DS}_1 | \mathrm{DS}_0, IM)$.

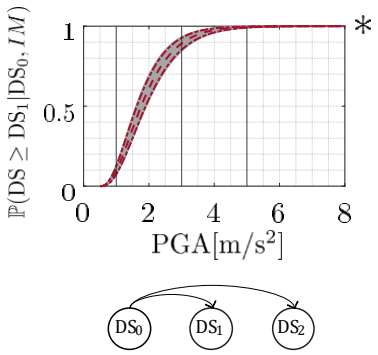

Figure B.1: The commonly used "fragility function" evaluated as the exceedance probability, i.e., $\mathbb{P}(\mathrm{DS} \geq \mathrm{DS}_1 | \mathrm{DS}_0, IM)$, for PGA as IM.

C - SPIF #2 support material.

C.1 Collection of the optimal state-dependent functions for each transition state.

The optimal IMs for each transition state were determined according to the β_{eff} index of Eq. 7. Table 10 collects the top-five-ranked IMs for each transition state. It is possible to notice that the Fajfar intensity $\mathrm{I_F}$, the equipment relative average spectral acceleration E-$\mathrm{ASA_{R67}}$, and the cumulated energy $\mathrm{E_{cum}}$ are the optimal IMs that occur more often among the transition states. Specifically, the $\mathrm{E_{cum}}$ and the E-$\mathrm{ASA_{R67}}$ are directly correlated with acceleration and energy content (see how they are defined in Table 1); whilst the $\mathrm{I_F}$ is correlated with velocity terms. Besides, the E-$\mathrm{ASA_{R67}}$ is the only one that is repeated on all the transition states. As deeply investigated in De Biasio et al. (2015a), this IM is particularly suited to capture the drop and frequency shifts of equipment characterised by a significant spectral acceleration close to the dominant frequency interval of the main structure. These observations agree with the experimental evidence described in Nardin et al. (2022). Indeed, the shake table data revealed a significant positive correlation between the maximum floor spectral acceleration $S_{a,floor}(T_1)$ and the E-$\mathrm{ASA_{R67}}$ for the vertical tank. Thus, Figure C.1 reports the state-dependent fragility functions for the industrial component with the optimal IM for each transition state. Dark-red lines and the associated shaded areas highlight the 50%, 90% and 99% confidence bounds, respectively. As the structure reaches the damage level $\mathrm{DS_2}$, $\mathrm{E_{cum}}$ is the optimal IM for both pristine and damaged initial level conditions. It can be noted that given a damage limit state to attain, i.e., (graphically) for elements of the same column, the magnitude of IM required to reach the same exceedance probability is lower with the damaged initial conditions. For instance, the

50% probability of exceedance DS_2 given DS_0 and DS_1 is associated to $E_{cum} = 9$ and $E_{cum} = 3$, respectively.

Table 10: Top five-ranked IM β_{eff} efficiency indices for each transition state.

Frag. '0-0' **Optimal IM**	β_{eff} **index**	**Frag. '0-1'** **Optimal IM**	β_{eff} **index**	**Frag. '0-2'** **Optimal IM**	β_{eff} **index**	**Frag. '1-1'** **Optimal IM**	β_{eff} **index**	**Frag. '1-2'** **Optimal IM**	β_{eff} **index**
I_F	5.00E-04	I_F	2.00E-04	E_{cum}	1.02E-04	I_F	3.00E-04	E_{cum}	6.96E-04
PGA	1.24E-02	E_{cum}	7.00E-04	I_A	9.25E-06	PGA	6.90E-03	$Sv(T_1)$	4.46E-03
I_C	3.75E-02	I_A	3.80E-03	I_C	6.58E-06	E_{cum}	4.14E-02	PGA	3.15E-03
$I_{RG,a}$	5.35E-02	E-ASA_{R67}	6.70E-03	I_{CM}	5.82E-06	$I_{RG,a}$	7.94E-02	E − ASA_{R67}	2.58E-03
E − ASA_{R67}	8.51E-02	PGA	1.60E-02	E-ASA_{R67}	1.81E-06	E-ASA_{R67}	9.55E-02	E-ASA_{R100}	6.19E-02

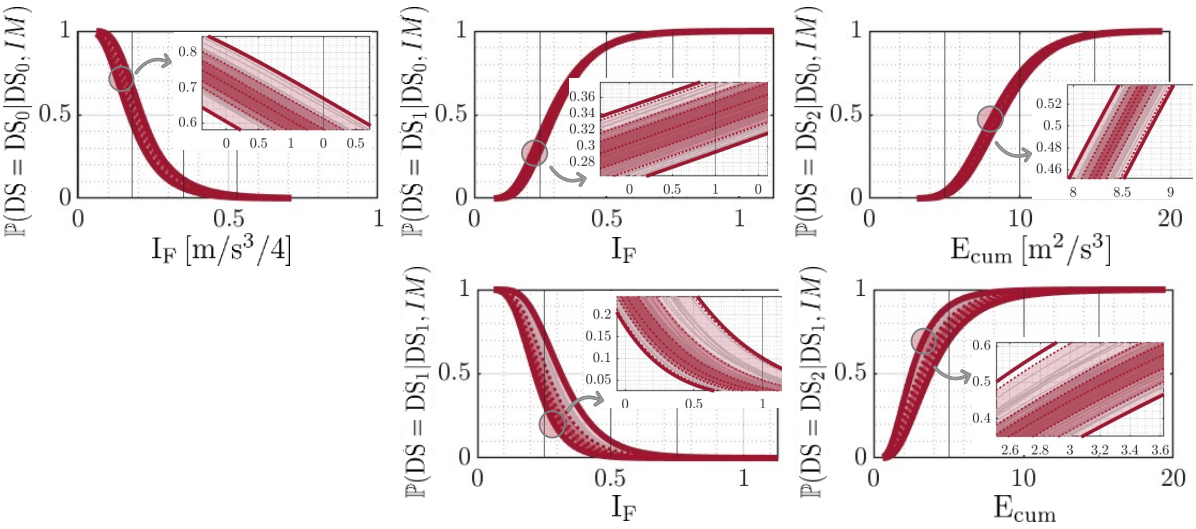

Figure C.1: Bootstrap-PCE state-dependent fragility curves of the SPIF #2 vertical tank: dark-red thick lines stand for the 50%, 90% and 99% confidence bound, along with lighter to darker shaded areas.

C.2 State-dependent fragility: $\mathbb{P}(DS \geq DS_1|DS_0, IM)$.

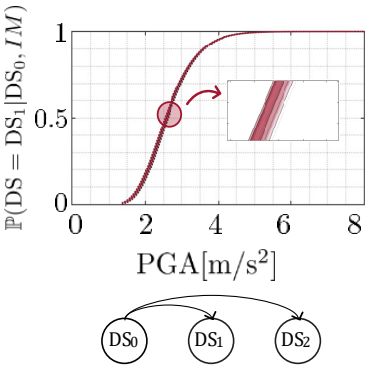

Figure C.2: The commonly used "fragility function" evaluated as the exceedance probability, i.e., $\mathbb{P}(\mathrm{DS} \geq \mathrm{DS}_1|\mathrm{DS}_0, IM)$, with PGA as IM.

References

Abbiati, G., M. Broccardo, I. Abdallah, S. Marelli, and F. Paolacci (2021). Seismic fragility analysis based on artificial ground motions and surrogate modeling of validated structural simulators. *Earthquake Engineering & Structural Dynamics 50*(9), 2314–2333.

Abdelnaby, A. E. (2018). Fragility curves for rc frames subjected to tohoku mainshock-aftershocks sequences. *Journal of Earthquake Engineering 22(5)*, 902–920.

Agency, F. E. M. (2000). Prestandard and commentary for seismic rehabilitation of buildings. *FEMA-356*.

Blatman, G. and B. Sudret (2008). Sparse polynomial chaos expansions and adaptive stochastic finite elements using a regression approach. *Comptes Rendus Mécanique 336*(6), 518–523.

Burton, H. V., G. Deierlein, D. Lallemant, and T. Lin (2016). Framework for incorporating probabilistic building performance in the assessment of community seismic resilience. *Journal of Structural Engineering 142*(8), C4015007.

Butenweg, C. et al (2020). *Seismic performance of multi-component systems in special risk industrial facilities. Deliverable D10.1, SERA Project, Project. No: 730900, H2020-EU*.

Cimellaro, G., A. Reinhorn, and M. Bruneau (2010, 11). Framework for analytical quantification of disaster resilience. *Engineering Structures 32*, 3639–3649.

De Biasio, M., S. Grange, F. Dufour, F. Allain, and I. Petre-Lazar (2015a). Intensity measures for probabilistic assessment of non-structural components acceleration demand. *Earthquake Engineering & Structural Dynamics*.

De Biasio, M., S. Grange, F. Dufour, F. Allain, and I. Petre-Lazar (2015b). *Intensity measures for probabilistic assessment of non-structural components acceleration demand. Earthquake Engineering & Structural Dynamics*.

De Rocquigny, E., N. Devictor, S. Tarantola, Y. Lefebvre, N. Pérot, W. Castaings, F. Mangeant, C. Schwob, R. Lavin, J.-R. Masse, P. Limbourg, W. Kanning, and P. Gelder (2008). *A guide*

to quantitative uncertainty management. John Wiley & Sons, Ltd.

Di Maio, F., F. Matteo, G. Carlo, F. Perotti, and E. Zio (2020, 08). Time-dependent reliability analysis of the reactor building of a nuclear power plant for accounting of its aging and degradation. *Reliability Engineering & System Safety 205*, 107173.

Du, A., J. Cai, and S. Li (2021). Metamodel-based state-dependent fragility modeling for markovian sequential seismic damage assessment. *Engineering Structures 243*, 112644.

Du, A. and J. E. Padgett (2020). Investigation of multivariate seismic surrogate demand modeling for multi-response structural systems. *Engineering Structures 207*, 110210.

Eads, L., E. Miranda, H. Krawinkler, and D. Lignos (2013, 01). An efficient method for estimating the collapse risk of structures in seismic regions. *Earthquake Engineering & Structural Dynamics 42*.

FEMA (2015). NEHRP. *Recommended Seismic Provisions for New Buildings and Other Structures*.

Filiatrault, A., C. Christopoulos, and C. Stearns (2001). Guidelines, specifications and seismic performance characterization of nonstructural building components and equipment. *PEER Report 2002/05, University of California, Berkeley, CA*.

Gentile, R. and C. Galasso (2020, 07). Gaussian process regression for seismic fragility assessment of building portfolios. *Structural Safety 87*.

Ghosh, J. and J. E. Padgett (2010). Aging considerations in the development of time-dependent seismic fragility curves. *Journal of Structural Engineering 136*(12), 1497–1511.

Hariri-Ardebili, M. and V. Saouma (2016). Probabilistic seismic demand model and optimal intensity measure for concrete dams. *Structural Safety 59*, 67–85.

Haukaas, T. and A. Der Kiureghian (2003, 01). Finite element reliability and sensitivity methods for performance-based engineering. *Pacific Earthquake EngineeringResearch Center, PEER*.

Hurtado, J. E. (2007). Filtered importance sampling with support vector margin: A powerful method for structural reliability analysis. *Structural Safety 29*(1), 2–15.

Iervolino, I. (2017). Assessing uncertainty in estimation of seismic response for pbee. *Earthquake Engineering & Structural Dynamics 46*(10), 1711–1723.

Iervolino, I., M. Giorgio, and E. Chioccarelli (2015, 11). Markovian modeling of seismic damage accumulation. *Earthquake Engineering & Structural Dynamics 45*, 441–461.

Ioannou, I., T. Rossetto, and D. Grant (2012). Use of regression analysis for the construction of empirical fragility curves.

Jia, G. and P. Gardoni (2018). State-dependent stochastic models: A general stochastic framework for modeling deteriorating engineering systems considering multiple deterioration processes and their interactions. *Structural Safety 72*, 99–110.

Kassem, M. M., F. M. Nazri, L. J. Wei, C. G. Tan, S. Shahidan, and S. S. M. Zuki (2019). Seismic fragility assessment for moment-resisting concrete frame with setback under repeated earthquakes. *Asian Journal of Civil Engineering 20*, 465–477.

Lu, Q. and W. Zhang (2021, 12). Integrating dynamic bayesian network and physics-based modeling for risk analysis of a time-dependent power distribution system during hurricanes. *Reliability Engineering & System Safety 220*, 108290.

Lüthen, N., S. Marelli, and B. Sudret (2021, 01). Automatic selection of basis-adaptive sparse polynomial chaos expansions for engineering applications. *International Journal for Uncertainty Quantification 12*.

Marelli, S., N. Lüthen, and B. Sudret (2022). UQLab user manual – Polynomial chaos expansions. Technical report, Chair of Risk, Safety and Uncertainty Quantification, ETH Zurich, Switzerland. Report UQLab-V2.0-104.

Marelli, S. and B. Sudret (2017). An active-learning algorithm that combines sparse polynomial chaos expansions and bootstrap for structural reliability analysis. *Structural Safety 75*.

Mosqueda, G., R. Retamales, A. Filiatrault, and A. Reinhorn (2009). Testing facility for experimental evaluation of non-structural components under full-scale floor motions. *The Structural Design of Tall and Special Buildings*.

Moustapha, M., S. Marelli, and B. Sudret (2022, 01). Active learning for structural reliability: Survey, general framework and benchmark. *Structural Safety 96*, 102174.

Nardin, C., O. S. Bursi, F. Paolacci, A. Pavese, and G. Quinci (2022). Experimental performance of a multi-storey braced frame structure with non-structural industrial components subjected to synthetic ground motions. *Earthquake Engineering & Structural Dynamics 51*(9), 2113–2136.

NIST GCR 17-917-44 (2017). *Seismic Analysis, Design, and Installation of Nonstructural Components and Systems – Background and Recommendations for Future Work. Applied Technology Council*.

Perez-Cruz, F. (2008, 08). Kullback-leibler divergence estimation of continuous distributions. pp. 1666 – 1670.

Quinci, G., C. Nardin, F. Paolacci, and O. Bursi (2023, 02). Modelling issues in seismic risk analysis of non-structural components located on industrial plant subsystems. *Bulletin Earthquake Engineering*.

Rezaeian, S. and A. Der Kiureghian (2010). *Simulation of synthetic ground motions for specified earthquake and site characteristics. Earthquake Engineering & Structural Dynamics*.

Richardson, J., G. Bagchi, and R. Brazee (1980). The seismic safety margins research program of the US Nuclear Regulatory Commission. *Nuclear Engineering and Design 59*((1)), 15–25.

Rossetto, T., I. Ioannou, and D. Grant (2015). Existing empirical fragility and vulnerability functions: Compendium and guide for selection. *GEM Technical Report*.

Rossi, L., M. Stupazzini, D. Parisi, B. Holtschoppen, G. Ruggieri, and C. Butenweg (2020, 03). Empirical fragility functions and loss curves for italian business facilities based on the 2012 emilia-romagna earthquake official database. *Bulletin of Earthquake Engineering 18*, 1–29.

Roy, A. and S. Chakraborty (2023, 05). Support vector machine in structural reliability analysis: A review. *Reliability Engineering & System Safety 233*, 109126.

Sudret, B. (2007). *Uncertainty propagation and sensitivity analysis in mechanical models - Contributions to structural reliability and stochastic spectral methods*. Hab. a diriger des recherches, Universite Blaise Pascal, Clermont-Ferrand, France.

Sudret, B. (2008). Global sensitivity analysis using polynomial chaos expansions. *Reliability Engineering & System Safety 93*(7), 964–979.

Sudret, B., S. Marelli, and J. Wiart (2017). Surrogate models for uncertainty quantification: An overview. In *2017 11th European Conference on Antennas and Propagation (EUCAP)*, pp. 793–797.

Teixeira, R., M. Nogal, and A. O'Connor (2021). Adaptive approaches in metamodel-based reliability analysis: A review. *Structural Safety 89*, 102019.

Vathi, M., S. Karamanos, I. Kapogiannis, and K. Spiliopoulos (2017, 05). *Performance Criteria for Liquid Storage Tanks and Piping Systems Subjected to Seismic Loading. Journal of Pressure Vessel Technology 139.*

Zentner, I., M. Gündel, and N. Bonfils (2017). Fragility analysis methods: Review of existing approaches and application. *Nuclear Engineering and Design 323.*

Zhang, Y., H. V. Burton, H. Sun, and M. Shokrabadi (2018). A machine learning framework for assessing post-earthquake structural safety. *Structural Safety 72*, 1–16.

Zhu, X., M. Broccardo, and B. Sudret (2023). Seismic fragility analysis using stochastic polynomial chaos expansions. *Probabilistic Engineering Mechanics 72*, 103413.